SUPPLEMENTARY INFORMATION

doi:10.1038/nature19797

List of Acronyms

Ag/Waste/LF	Agriculture, waste, landfills (microbial CH_4 source subcategory)
CH_4	Methane
BB	Biomass burning (CH_4 source category; including wildfires and biofuels)
FER	Fugitive emission rate (fraction of natural gas production lost to the atmosphere through its lifecycle, i.e., production, processing, transport, and use)
FF	Fossil fuels (natural gas, oil, coal)
FF_{Geo}	Natural geological CH_4 seepage (FF CH_4 source subcategory)
FF_{Ind}	CH_4 emissions from the natural gas, oil, and coal industries (FF CH_4 source subcategory)
FF_{Tot}	FF_{Geo} + FF_{Ind}
IAV	Inter-annual variability
MC	Monte Carlo (statistical method for repeated random sampling)
NG	Natural gas
$\delta^{13}C_{Atm}$	Atmospheric $\delta^{13}C$–CH_4
$\delta^{13}C_{BB}$	$\delta^{13}C$–CH_4 source signature of BB
$\delta^{13}C_{FF}$	$\delta^{13}C$–CH_4 source signature of FF
$\delta^{13}C_{Mic}$	$\delta^{13}C$–CH_4 source signature of microbial sources
$\delta^{13}C_{Source}$	$\delta^{13}C$–CH_4 source signature (generic)

1. Box-model

Time series (1984-2013) distributions of global CH_4 from FF_{Tot}, FF_{Geo}, and global average FER were estimated using an atmospheric mass balance approach (1-box-model, i.e., conservation of mass). Total annual CH_4 emissions $Q_{Atm,t}$ in year t based on atmospheric observations and estimates of CH_4 sinks are calculated using Eq. 2, which is the digitized solution to differential Eq. 1, solved for $Q_{Atm,t}$ (centered on the time derivative).

$$\frac{dX_{CH4}}{dt} = Q_{Atm,t} - \frac{X_{CH4,t}}{\tau} \quad \textbf{Eq. 1,}$$

$$Q_{Atm,t} = \frac{X_{CH4,t} - X_{CH4,t-1}}{\Delta t} + \frac{X_{CH4,t} + X_{CH4,t-1}}{2\tau} \quad \textbf{Eq. 2,}$$

where $X_{CH4,t}$ is the annual mean, globally averaged CH_4 mole fraction (see data in SI section 2) multiplied by 2.767 Tg CH_4/ppb (ref[31,32]), Δt is one year, and τ is the global average atmospheric CH_4 lifetime (tropospheric OH and stratospheric sink; see Eq. 8 for soil sink treatment). For τ, a range of 8.6-9.4 years (10^{th}/90^{th} percentiles) was chosen based on five studies[32–36] as described below. Inter-annual variability (IAV) in the OH abundance may affect global total CH_4 emissions and source attribution in a specific year (±2%, i.e. ~±11 Tg CH_4/yr, ref[37]), and while there may be long-term changes in the global OH abundance over the last 30 years, there is no observational evidence for it[38]. This study's primary interest is the partitioning of sources into broad categories and their long-term trends, and we did not account for IAV of OH. The ^{13}C:^{12}C ratio of CH_4, expressed as the dimensionless $\delta^{13}C$, is defined[39] as $\delta^{13}C = R_{Sample}/R_{Standard} - 1$, where R is defined as the isotopic ratio $^{13}C/^{12}C$. The change in the atmospheric ^{13}C-CH_4 mole fraction $d(X_{CH4}\, R_{Atm})/dt$ is estimated using Eq. 3 and Eq. 4:

$$\frac{d(X_{CH4}\, R_{Atm})}{dt} = R_{Atm,t}\frac{dX_{CH4}}{dt} + X_{CH4,t}\frac{dR_{Atm}}{dt} \quad \textbf{Eq. 3,}$$

$$\frac{d(X_{CH4}\, R_{Atm})}{dt} = Q_{Atm,t}R_{Q,t} - (1+\varepsilon)\frac{X_{CH4,t}R_{Atm,t}}{\tau} \quad \textbf{Eq. 4,}$$

where ε is the isotopic fractionation factor[40] associated with photochemical methane destruction (see SI Table 1 for ε parameter values). Substituting Eq. 3 and Eq. 4, dividing by $R_{Standard}$, and substituting $\delta^{13}C = R_{Sample}/R_{Standard} - 1$ yields

$$X_{CH4}\frac{d\delta^{13}C_{Atm}}{dt} = Q_{Atm,t}\left(1+\delta^{13}C_{Q,t}\right) - \left((1+\varepsilon)\frac{X_{CH4,t}}{\tau} + \frac{dX_{CH4,t}}{dt}\right)\left(1+\delta^{13}C_{Atm,t}\right) \quad \textbf{Eq. 5,}$$

where $\delta^{13}C_{Q,t}$ is the flux weighted mean isotopic ratio of all CH_4 sources. The global average $\delta^{13}C_{Atm,t}$ data are described in SI section 2. Substituting Eq. 1 in Eq. 5 yields

$$X_{CH4}\frac{d\delta^{13}C_{Atm}}{dt} = Q_{Atm,t}\left(1+\delta^{13}C_{Q,t}\right) - \left((1+\varepsilon)\frac{X_{CH4,t}}{\tau} + Q_{Atm,t} - \frac{X_{CH4,t}}{\tau}\right)\left(1+\delta^{13}C_{Atm,t}\right) \quad \textbf{Eq. 6.}$$

Solving for $\delta^{13}C_{Q,t}$ yields

$$\delta^{13}C_{Q,t} = \delta^{13}C_{Atm,t} + \frac{\varepsilon\left(1+\delta^{13}C_{Atm,t}\right)}{Q_{Atm,t}}\frac{X_{CH4,t}}{\tau} + \frac{d\delta^{13}C_{Atm}}{dt}\frac{X_{CH4,t}}{Q_{Atm,t}} \quad \textbf{Eq. 7}.$$

The global mass balance for three CH_4 source categories and the soil sink were formulated for each year based on refs[40,41]:

$$Q_{Atm,t} = Q_{Mic,t} + Q_{FF,tot,t} + Q_{BB} + Q_{Soil} \quad \textbf{Eq. 8,}$$

$$\delta^{13}C_{Q,t}\,Q_{Atm,t} = \delta^{13}C_{Mic}\,Q_{Mic,t} + \delta^{13}C_{FF,t}Q_{FF,tot,t} + \delta^{13}C_{BB}\,Q_{BB} + \delta^{13}C_{Q,t}\,Q_{Soil} \quad \textbf{Eq. 9}.$$

The parameters $\delta^{13}C_{\mathrm{Mic}}$, $\delta^{13}C_{\mathrm{FF,t}}$, and $\delta^{13}C_{\mathrm{BB}}$ refer to microbial (Ag/Waste/LF and other biogenic sources), $\mathrm{FF_{Tot}}$, and BB specific source signatures, respectively. The parameters $Q_{Mic,t}$, $Q_{FF,Tot,t}$, and Q_{BB} refer to the respective total annual CH_4 emissions, and Q_{Soil} is the global soil sink (negative). See SI Table 1 for model input distributions of Q_{BB}, Q_{Soil}, $\delta^{13}C_{Mic}$, $\delta^{13}C_{FF,t}$, and $\delta^{13}C_{BB}$. The input parameters Q_{BB} (including both wild fires and biofuels), Q_{Soil}, $\delta^{13}C_{Mic}$, and $\delta^{13}C_{BB}$ are treated constant over time (i) due to data unavailability, and (ii) because there is no evidence of a trend of these parameters. Unaccounted IAV of these parameters may affect model results for individual years, but this study focuses on long-term trends, and does not draw conclusions about emissions from individual years. The different CH_4 sources are aggregated to only three categories to avoid an under-constrained system of two linear equations (Eq. 8 and Eq. 9). The equation system is solved for $Q_{Mic,t}$ and $Q_{FF,Tot,t}$ (Eq. 10 and Eq. 11):

$$Q_{FF,Tot,t} = \frac{\delta^{13}C_{Q,t}\left(Q_{Atm,t} - Q_{Soil}\right) - \delta^{13}C_{Mic}\left(Q_{Atm,t} - Q_{BB} - Q_{Soil}\right) - \delta^{13}C_{BB}\,Q_{BB}}{\delta^{13}C_{FF,t} - \delta^{13}C_{Mic}} \quad \textbf{Eq. 10,}$$

$$Q_{Mic,t} = Q_{Atm,t} - Q_{FF,Tot,t} - Q_{BB} - Q_{Soil} \quad \textbf{Eq. 11},$$

where all Q are Tg CH_4/yr. We also applied this box-model to pre-industrial ice-core CH_4 and $\delta^{13}C_{\mathrm{Ice}}$ data in combination with our $\delta^{13}C_{\mathrm{Source}}$ database to estimate the portion of $Q_{FF,Tot,t}$ due to geological seepage, $Q_{FF,Geo}$, to compare with the literature (SI section 6). CH_4 emissions from NG, $Q_{FF,NG,t}$, are calculated by subtracting $Q_{FF,Geo}$ and bottom-up estimates[28] (including uncertainties) of coal (including "other industrial" emissions) and oil emissions (SI Table 1) from $Q_{FF,Tot,t}$:

$$Q_{FF,NG,t} = Q_{FF,Tot,t} - Q_{FF,Coal,t} - Q_{FF,Oil,t} - Q_{FF,Geo} \quad \textbf{Eq. 12}.$$

Parameters $Q_{FF,Tot,t}$ and $Q_{FF,Geo}$ were modeled with a correlation coefficient of 1 for box-model MC simulations because both are constrained by the same type of observations and model parameters with similar (and sometimes the same) values and uncertainty ranges. The correlation coefficient of 1 slightly underestimates the uncertainty in $Q_{FF,NG,t}$ because the Q_{BB} term has a slightly smaller contribution to the modern CH_4 budget (8%; SI Table 1) than the paleo budget (11%; SI section 6). All other parameters in the box-model were assumed uncorrelated. Finally, we estimate FER as a function of time:

$$FER_t = \frac{Q_{FF,NG,t}}{P_{dry,t}\, WF_{down,CH4,t}} \qquad \textbf{Eq. 13,}$$

where $P_{dry,t}$ is the global dry gas production of NG[16] (see the FF_{Ind} bottom-up inventory[28] for details), and $WF_{down,CH4,t}$ is the downstream dry NG CH_4 mass fraction (ref[28]; see also SI Table 1). All model parameter input distributions are summarized in SI Table 1. Discrete distributions were used depending on availability of literature data. Global mean CH_4 lifetimes (tropospheric and stratospheric sinks) and standard deviations from five studies[32–36] assuming underlying normal distributions were used in a MC simulation to generate a discrete distribution for the box-model (SI section 2). Discrete isotopic signature distributions were established based on our global $\delta^{13}C_{Source}$ inventory compiled from the literature (SI section 3–5). For all other parameters, $10^{th}/90^{th}$ percentiles were estimated based on minimum and maximum literature values, and underlying normal distributions were assumed except for $Q_{Oil,t}$ (gamma distribution used to account for skewed literature values).

Forward simulations of CH_4 levels using the global atmospheric chemistry and transport model TM5[27] cover 1980-2012. While CH_4 observations start in 1984, the first four years allow for model initialization (spatial and vertical mixing from initialized conditions). We simulated CH_4 levels arising from 11 individual source/sink categories (NG, oil, coal/industry, wetlands, soils, oceans, termites, wild animals, AG/Waste/LF, and BB), and the CH_4 fluxes of existing grid maps were scaled to match the total CH_4 emissions consistent with multiple scenarios from the box model (see SI section 8 for simulation details).

SI Table 1: Parameters and input distributions used in the MC simulation for 1984-2013. Oil and coal emission estimates are illustrated for selected years throughout the analysis time frame (see references for all years). Note that τ, δ, Q_{BB}, and Q_{Soil} are the key parameters for quantifying total FF emissions $Q_{FF,Tot,t}$ (Eq. 1 through Eq. 11), which is then used to estimate FER based on the remaining parameters (Eq. 12 and Eq. 13).

Parameter		Distribut-ion type [a]	Mean	10th Percentile	90th Percentile	Refs.
Global mean CH_4 lifetime (Years) [b]						
	τ	Discrete	9.0	8.6	9.4	SI section 2
Isotopic signatures (‰) [c]						
Microbial (N = 1,021) [d]	$\delta^{13}C_{Mic}$	Discrete	-62.2	-63.2	-61.2	SI section 3
Biomass burn. (N = 965) [d]	$\delta^{13}C_{BB}$	Discrete	-22.2	-24.7	-20.0	SI section 4
Fossil fuels (N = 7,482) [e]	$\delta^{13}C_{FF}$	Discrete	-44.0	-44.9	-43.2	SI section 5
Isotopic fractionation factor (‰) [f]	ε	Normal	-6.3	-7.1	-5.5	40
Soil sink and sources						
Soil sink	Q_{Soil}	Normal	-32	-34	-30	11
Biomass burning [g]	Q_{BB}	Normal	43	31	55	11
Geological seepage [h]	$Q_{FF,Geo}$	Discrete	50	22	78	SI section 6
Oil, bottom-up, 2011			20	6	38	
2000	$Q_{FF,Oil,t}$	Gamma	19	5	37	28
1990			16	4	32	
Coal [i], bottom-up, 2011			66	59	72	
2000	$Q_{FF,Coal,t}$	Normal	45	38	51	28
1990			51	45	58	
NG composition (wt-%)						
Downstream NG CH_4 content	$WF_{down,CH4,t}$	Normal	86	85	87	28

Notes: [a] Discrete distributions based on MC simulations using multiple literature estimates. Other distribution types according to literature availability. [b] Includes OH and stratospheric sinks. [c] All data in the $\delta^{13}C_{Mic}$, $\delta^{13}C_{BB}$ and $\delta^{13}C_{FF}$ isotopic source signature databases are referenced to the common Pee Dee Belemnite (PDB)/Vienna Pee Dee Belemnite (VPDB) scale (ref[42]). [d] MC simulation results. [e] Temporal average distribution based on MC simulation. [f] Includes OH, soil, and stratospheric sinks. [g] Includes biofuels (biomass fuel combustion) and wild fires. [h] $Q_{FF,Geo}$ and $Q_{FF,Tot,t}$ were modeled with correlation coefficient of 1 in Eq. 11. [i] Includes ~19 Tg CH_4/yr "Other industry" emissions (EDGAR v4.2[2]).

2. Atmospheric measurements

Methane measurements from air samples collected within NOAA's Global Greenhouse Gas Reference Network were used for 1984–2013[20]. A map of the 84 surface air sampling sites is presented in SI Figure 1.

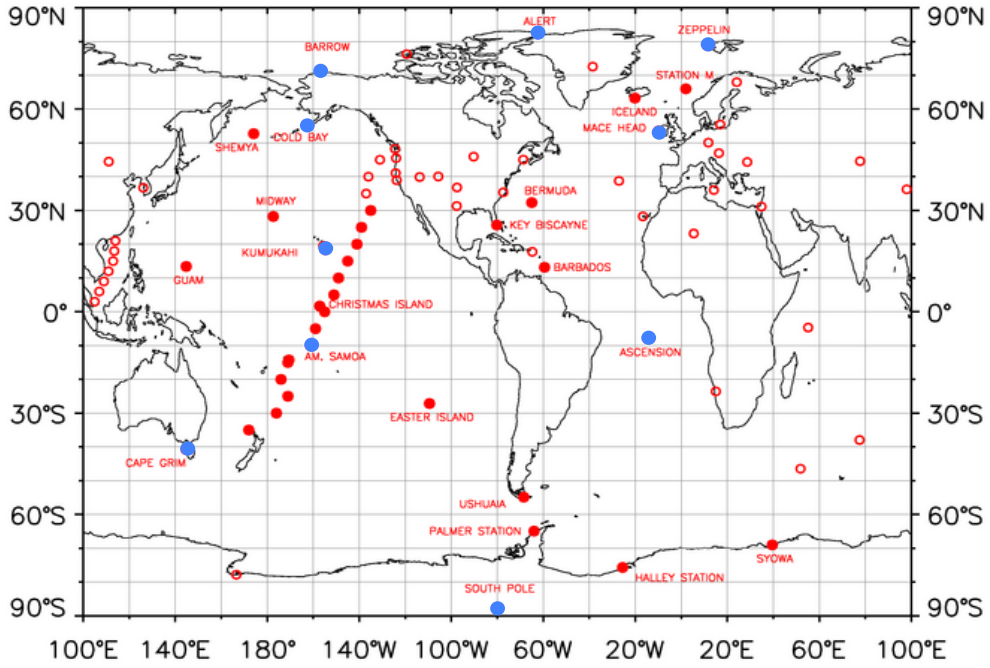

SI Figure 1: NOAA Global Monitoring Division's Global Greenhouse Gas Reference Network[20] providing CH_4 measurements at each site. Filled circles represent well-mixed marine boundary layer air sites used to calculate global mean CH_4. Sites used to calculate global mean $\delta^{13}C_{Atm}$ are marked blue.

The box-model uses global average annual CH_4 levels based on measurements from a subset of the network sites shown as filled circles (global mean $\delta^{13}C_{Atm}$ was calculated from sites marked blue). These sites are typically at remote marine sea level locations, which are representative of well-mixed marine boundary layer air. Globally averaged annual mean CH_4 mole fractions are plotted in SI Figure 2 (left axis). The uncertainty in globally averaged annual mean CH_4 varies by year, but is <1 ppb (1 SD)[43]. This uncertainty accounts for potential biases from removing and adding sites in a MC simulation (see ref[44] for methods and uncertainties in calculating global means). Considering the wide uncertainty range of the CH_4 lifetime, this small uncertainty was considered negligible. The resulting total annual emissions, $Q_{Atm,t}$ (Eq. 2), are shown on the right axis of SI Figure 2 for CH_4 lifetimes τ (OH and stratospheric sinks; see SI Table 1 for soil sink) ranging from 8.6–9.4 years (10^{th}–90^{th} percentiles) based on the joint distribution from four recent

publications[32–35] (each individual τ distribution was assumed equally likely, and the stratospheric sink from Prinn *et al*.[34] was used when not specified[33,35]). Note that this distribution is nearly identical to the 9.0 years (+0.4, –0.6) in an earlier study by Montzka *et al*. (2000)[36].

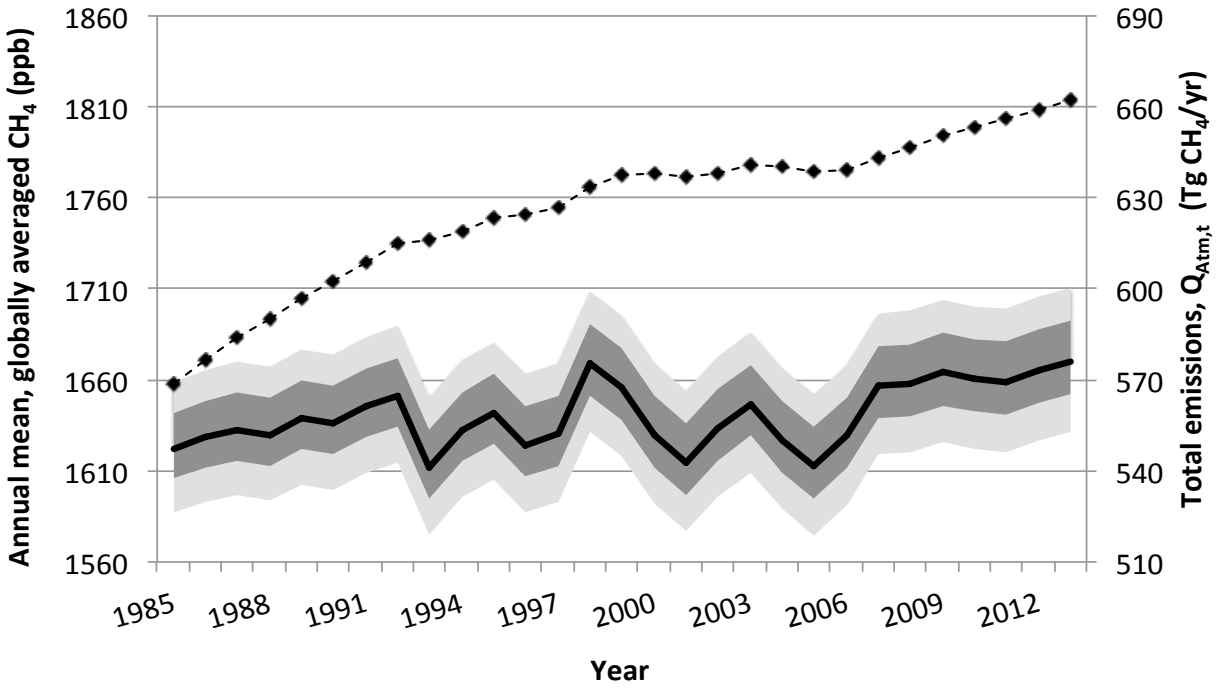

SI Figure 2: Annual mean, globally averaged CH_4 dry mole fractions (dashed, left axis) from NOAA[20]; ±1.1 ppb (1 SD) uncertainty, averaged across years[45,46]. Right axis shows total CH_4 emissions (dark and light gray bands mark the 25th/75th percentile and the 10th/90th percentile uncertainties, respectively) for the range of CH_4 lifetimes used in the box-model.

Global average $\delta^{13}C_{Atm}$ from INSTAAR/NOAA[45,47] are shown in SI Figure 3 for 1999–2013. We use global average 1984–1998 $\delta^{13}C_{Atm}$ data from Schaefer *et al*.[21], which increase by ~0.4‰ during this period. The box-model accounts for a $\delta^{13}C_{Atm}$ uncertainty of ±0.1‰, which includes uncertainties in measurement reproducibility (±0.07‰[47,48]) and in estimating global annual averages (marine boundary layer background site selection). As shown in SI Figure 17, the ±0.1‰ $\delta^{13}C_{Atm}$ uncertainty translates into only ~3 Tg CH_4/yr FF_{Tot} uncertainty and ~0.1 percentage point FER uncertainty. All data from Schaefer *et al*.[21] were adjusted to the INSTAAR $\delta^{13}C_{Atm}$ scale (~0.1‰ offset). Considering other internationally recognized labs, the largest possible $\delta^{13}C_{Atm}$ scale offset is 0.3‰ or less[48], although uncertainty relative to Vienna Pee Dee Belemnite (VPDB) is only ±0.1‰ (ref[49]). Summing the fractional uncertainties of $\delta^{13}C_{Atm}$ and the

scale offset (0.3‰) in quadrature results in ~9 Tg CH_4/yr FF_{Tot} uncertainty and ~0.3 percentage points FER uncertainty.

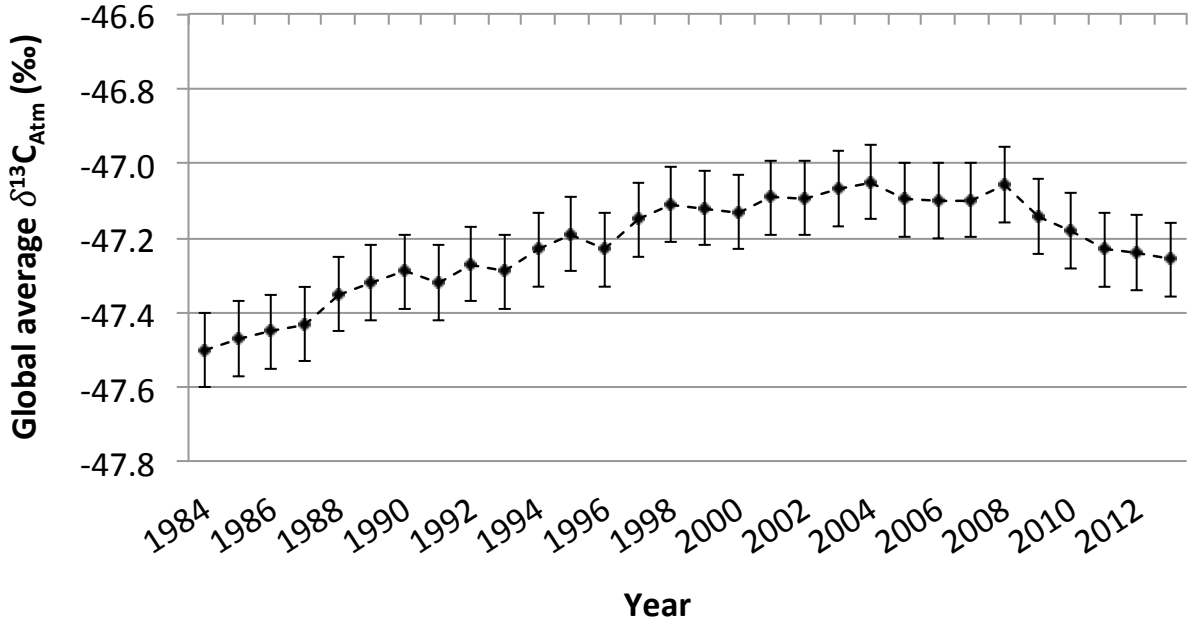

SI Figure 3: Annual mean, globally averaged $\delta^{13}C_{Atm}$ from INSTAAR/NOAA[45,47] (1999-2013) and Schaefer *et al.*[21] (Table S4 and Figure 1b; 1984-1998). All data are shown on the same INSTAAR $\delta^{13}C_{Atm}$ scale and used as such in the mass balance (see text details above).

3. Microbial isotopic source signature

A $\delta^{13}C_{Source}$ database including 1,021 $\delta^{13}C_{Mic}$ measurements was compiled from the literature for the following microbial source categories: wetlands, termites, ruminants, rice agriculture, and waste/landfills. The full database including measurement locations, means and uncertainties, sample sizes, metadata (e.g., season), and literature references is available in ref[14]. Measurement methods include flux chamber (e.g., wetlands) and downwind plumes (e.g., landfills). Each database entry describes an original set of measurements for a specific geographic area or date, or both. A $\delta^{13}C_{Mic}$ distribution was established for each microbial source sub-category by MC simulation sampling from each $\delta^{13}C_{Mic}$ literature entry within each sub-category (including mean and SD; see SI Figure 4).

Ruminant $\delta^{13}C_{Mic}$ data and weighting based on diet

Ruminant $\delta^{13}C_{Mic}$ measurements were distinguished by diet because CH_4 from a C_4 plant based diet is heavier than from a C_3 plant based diet based on our database[14]. It includes ruminant

$\delta^{13}C_{Mic}$ measurements with controlled diets, and the data indicate a bimodal distribution: diets consisting of ≥60% C_4 plants yield $\delta^{13}C_{Mic}$ of –54.6 ± 3.1‰ (1 SD) compared to a C_3 plant based diet (–69.4 ± 3.1‰). Weighting C_3 vs. C_4 based diet signatures requires global ruminant feed data including grains and grasses. Cattle contribute 96% of U.S. ruminant CH_4 emissions (the remainder being mainly pigs, horses, sheep, and goats)[22] even though cattle represent only 57% of U.S. ruminant livestock (1980–2013 average; the global figure is 33%[50]). Since cattle are by far the dominant ruminant source, and because of lack of diet data for other ruminants, this model does not account for potential differences in the C_3/ C_4 diet ratio between cattle and other ruminants.

The economically important C_4 grains used as cattle feed (including byproducts) include maize, sugarcane, sorghum, and millets, whereas most other grains are from C_3 plants. We estimated the fraction of U.S. cattle with a C_4-based diet (defined as ≥60% C_4 plants, see above) as follows. The majority of U.S. cattle feed C_4 grains include maize (94%) and sorghum (4%)[51]. Based on literature[52–54] and expert feedback[55], our model assumes 0–40% C_4 diet (uniform distribution) in cow-calf operations, 100% in feedlots, and 0–25% (uniform distribution) in dairy operations (all including C_4 grains and silage). Weighting the C_4 distributions of these operations by their relative emission strength[22] results in a U.S. C_4 emission fraction of 19.6 ± 5.9% (1 SD). Extrapolating the U.S. C_4 emission fraction globally, where there is little available data, requires accounting for the relatively high use of C_4 feed grain in the U.S. During 1980–2013, the U.S. held only 7% of the global cattle population[50], but it consumed 32% of global maize and sorghum feed[51]. We therefore used the U.S. C_4 emission fraction as a global upper bound. As a global lower bound, the model assumes that the C_4 diet fraction in the rest of the world (ROW) is zero, i.e., only a negligible fraction of ROW cattle receives C_4-based plant feed. Accounting for U.S. and global cattle populations[50] results in a global weighted average C_4 emission fraction range of 1.5–19.6% (uniform). Note that we assume a C_4 diet fraction for grazing cattle similar to our distribution for grain-fed cattle. This assumption is consistent with global plant coverage data indicating that ~20% of both total land and cropland coverage are C_4 based[56]. Thus, unless a disproportionately large fraction of cattle grazes on land with predominantly C_4 based vegetation, our global weighted average C_4 emission fraction distribution can be used to encompass both grain and grass based diets. Weighting the above C_3 and C_4 diet $\delta^{13}C_{Mic}$ distributions by the

respective emission fraction distributions in a MC simulation yields a global weighted average ruminant $\delta^{13}C_{Mic}$ of (-66.8 ± 2.8‰, 1 SD). The vast majority of ruminant $\delta^{13}C_{Mic}$ samples is from C_3 diets (159 out of 171), which is representative of the C_3 ruminant emissions fraction (80.4–98.5%, i.e., 100% minus C_4 fraction described above).

Wetland, termites, rice and landfill/waste $\delta^{13}C_{Mic}$ data and total microbial weighting

The wetland $\delta^{13}C_{Mic}$ contains 512 samples from 9 countries on 4 continents across seasons. The rice $\delta^{13}C_{Mic}$ contains 252 samples from 6 countries on 4 continents throughout the rice cultivation cycle. The landfill/waste $\delta^{13}C_{Mic}$ contains 57 landfill and manure samples from 4 countries in North America and Europe. The termite $\delta^{13}C_{Mic}$ contains 29 samples collected from natural termite nests and in lab experiments. The differences in sample sizes between these categories are roughly representative of their respective emissions strengths (see SI Figure 5). The individual $\delta^{13}C_{Mic}$ for wetlands (-61.5 ± 0.6‰), termites (-65.0 ± 1.7‰), rice (-62.1 ± 1.3‰) and landfill/waste (-55.6 ± 0.7‰) show significantly narrower distributions than for ruminants.

A weighted average microbial $\delta^{13}C_{Mic}$ distribution (representing the categories ruminants, wetland, termites, rice and landfill/waste) was estimated as illustrated in SI Figure 4. Discrete distributions of each source category from the database were weighted by their respective relative emissions (RE; percentage of global total microbial CH_4). A set of 12 RE literature estimates was used from two bottom-up study reviews[57,58] and four top-down inversion studies [3,4,6,7] to account for RE uncertainty. The resulting 12 weighted average $\delta^{13}C_{Mic}$ distributions were sampled in the MC simulation assuming equal weight of each distribution, which yielded a single weighted average $\delta^{13}C_{Mic}$ distribution.

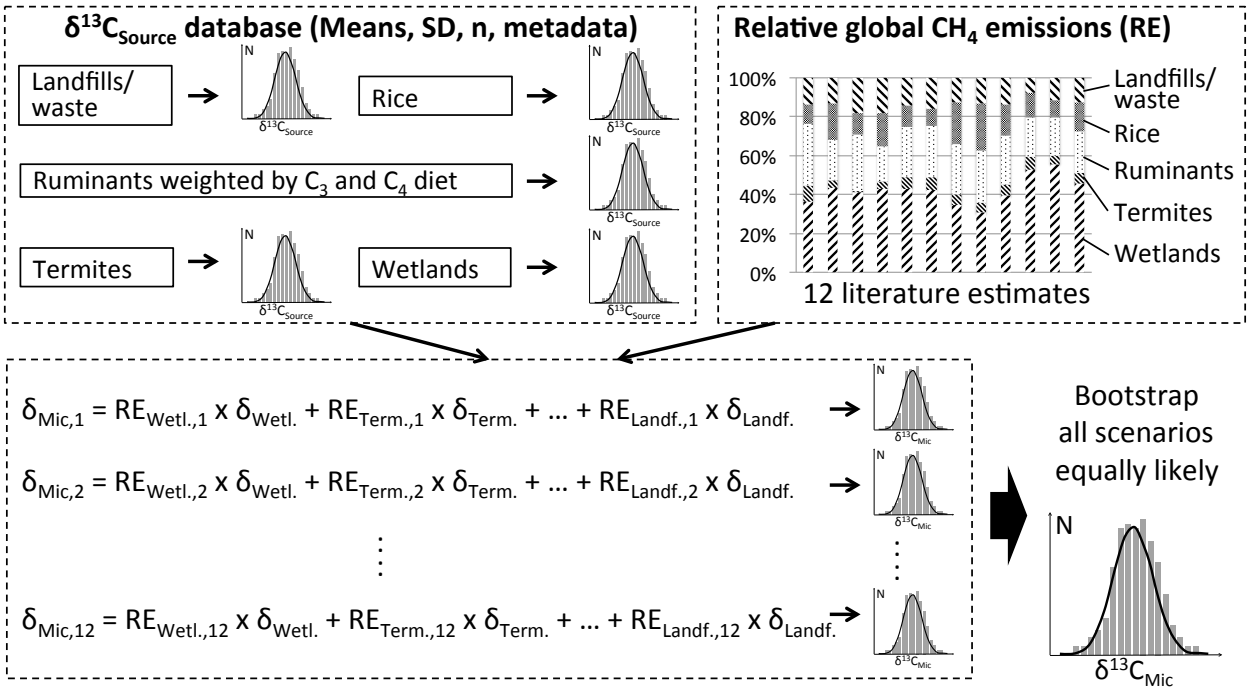

SI Figure 4: Methods overview for estimating the weighted average $\delta^{13}C_{Mic}$. Given the large uncertainty of the share of C_3 vs. C_4 ruminant diet, C_3 and C_4 ruminant diet $\delta^{13}C_{Mic}$ distributions were weighted according to the global C_3/ C_4 diet ratio (see text).

Ranges of global microbial CH_4 RE are shown in SI Figure 5 including average RE in red (mean of all 12 data points). The 12 RE estimates include (i) the lower and upper bound total microbial CH_4 emission scenarios from two bottom-up studies[57,58], and (ii) the prior and posterior CH_4 emission scenarios from four top-down studies[3,4,6,7]. The four top-down studies are based on different prior datasets as shown by the varying RE values, and there is no consistent bias between prior and posterior RE between studies. Wetlands and ruminants combined account on average for about 66% of total microbial source CH_4 emissions followed by rice agriculture and landfills/waste (14% each), and termites (5%).

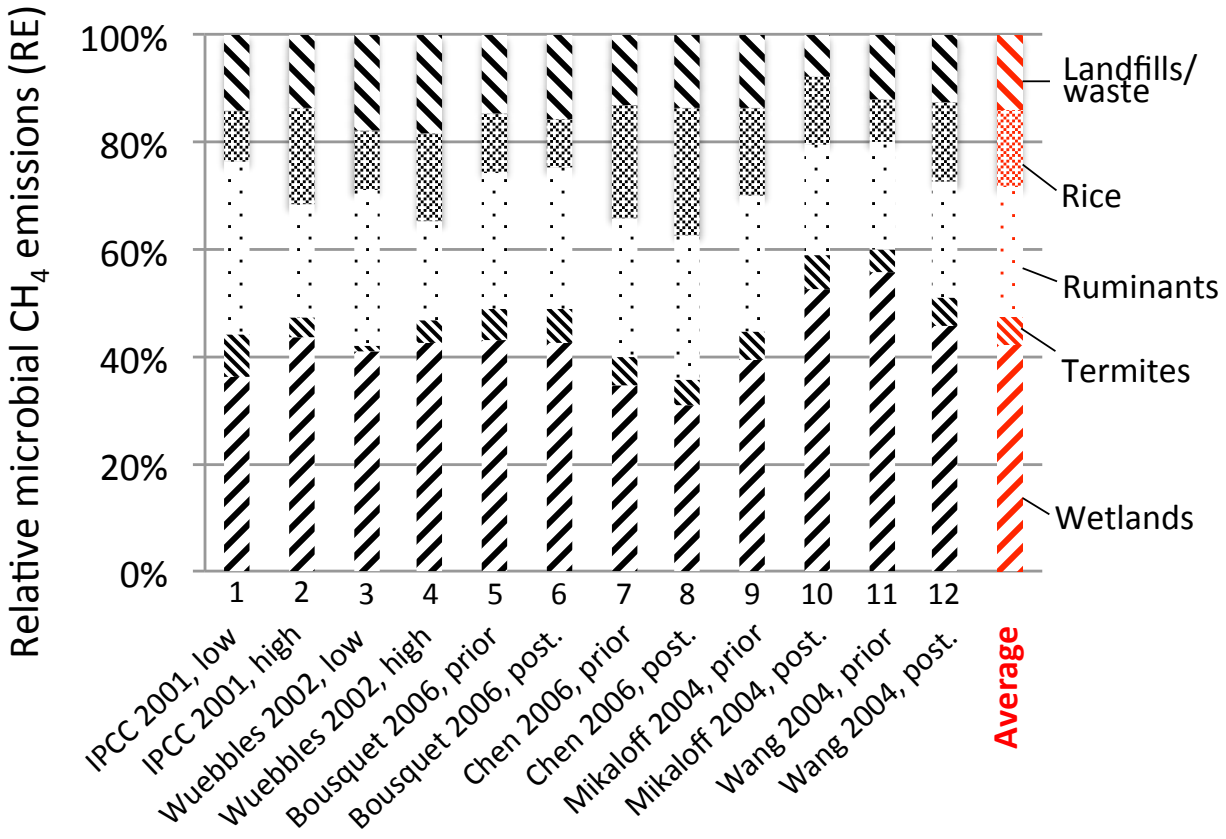

SI Figure 5: Contribution of sources to global total microbial CH_4 (relative emissions, RE) based on ranges from six studies[3,4,6,7,57,58] as well as the average contribution from all studies (red). The indices 1–12 refer to the weighted average $\delta^{13}C_{Mic}$ scenarios in SI Figure 6.

The $\delta^{13}C_{Mic}$ and 1 SD of individual source categories based on 1,021 individual measurements from 82 independent studies (i.e., unique location and/or date) and the resulting weighted averages are shown in SI Figure 6. The influence of RE uncertainty (SI Figure 5) on the weighted average microbial $\delta^{13}C_{Mic}$ distribution is small. The weighted average $\delta^{13}C_{Mic}$ difference between the highest (scenario 4) and lowest (scenario 1) is only 0.7‰. The resulting weighted average $\delta^{13}C_{Mic}$ is –62.2 ± 0.8‰ (1 SD).

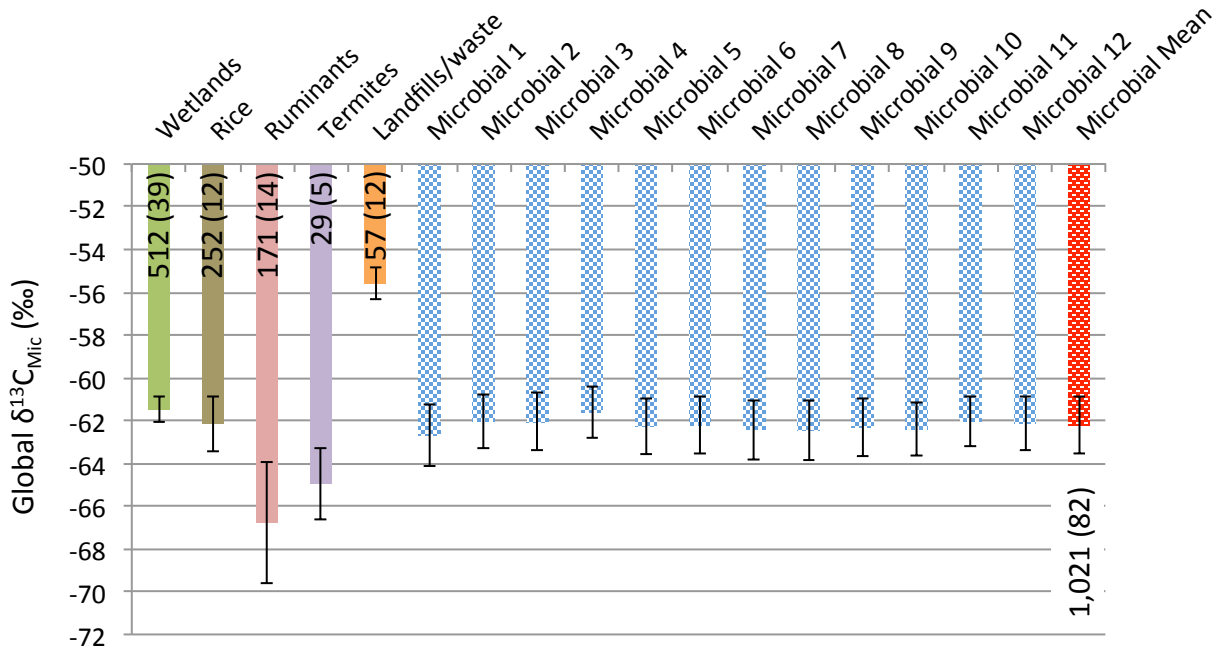

SI Figure 6: $\delta^{13}C_{Mic}$ and 1 SD uncertainties of individual source categories (solid) and weighted averages (hatched) based on the 12 scenarios in SI Figure 5. The microbial mean and 1 SD were estimated by MC simulation sampling of the distributions of all weighted averages. The sample sizes of each source category and the total are shown on the respective bars (values in parentheses indicate number of independent studies, i.e., unique location and/or date).

4. Biomass burning isotopic source signature

There are relatively few $\delta^{13}C_{BB}$ direct plume measurement data available globally. Our literature survey resulted in 82 individual samples from 22 studies. Only 22 samples from 8 studies (in Zambia and Brazil) are associated with tropical latitudes where the vast majority of global BB occurs according to satellite retrievals[59]. Only 6 samples from 2 studies are associated with C_4 plants (C_3 for the remainder). A list of all sample details and references is available in the supplementary data file. Given the significantly different C_3 and C_4 biomass plant material $\delta^{13}C_{BB}$, we also compared the direct measurements with 965 indirect measurements, i.e., $\delta^{13}C_{BB}$ in C_3 and C_4 plant material (grasses) from Cerling *et al*. 1997[60], to improve global data representativeness. The general procedure for estimating a weighted $\delta^{13}C_{BB}$ follows the schematic in SI Figure 7. Global C_3 and C_4 BB vegetation maps from Still *et al*. 2003[56] and GFED v1[23] were used in combination with global monthly (1997–2003 due to data availability) BB CH_4 flux maps from GFED v1 and v3[23] to estimate monthly C_3 and C_4 fractions of global

total BB CH_4 emissions (SI Figure 7, panel a). The four sets (two vegetation and flux maps each) of 84 monthly discrete C_3 and C_4 fractions were used in a MC simulation, assuming equal probability of all discrete values, to generate a distribution of C_3 and C_4 fractions (SI Figure 7, panel b). Distributions of the above direct and indirect measurements of C_3 and C_4 plant $\delta^{13}C_{BB}$ (SI Figure 7, panel c) were weighted with the C_3 and C_4 fraction distributions in a MC simulation to yield a distribution of the global weighted average $\delta^{13}C_{BB}$.

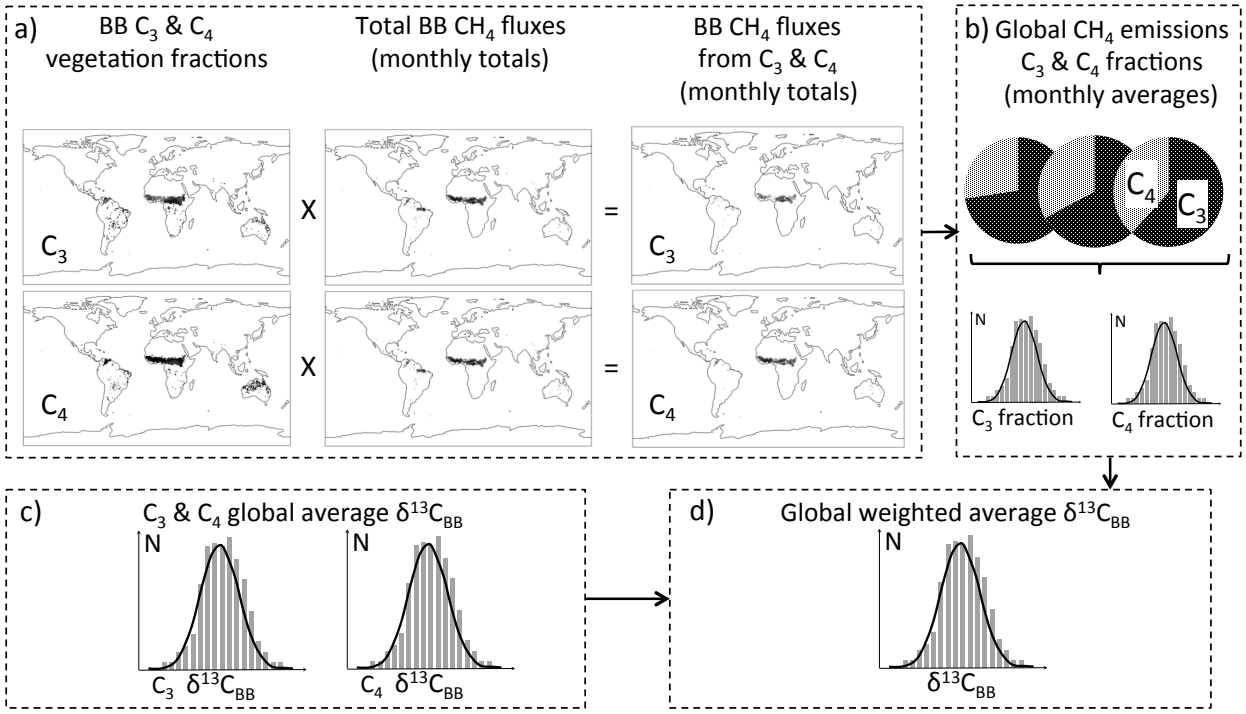

SI Figure 7: Weighting procedure for estimating a global weighted $\delta^{13}C_{BB}$ based on global C_3 and C_4 BB vegetation maps[23,56], global BB CH_4 flux maps[23], and literature C_3 and C_4 specific $\delta^{13}C_{BB}$.

The resulting $\delta^{13}C_{BB}$ are shown in SI Figure 8. Panel a) summarizes the C_4 plant fractions (temporal distributions from monthly data) for each combination of plant maps and BB CH_4 flux maps as well as their average from the MC simulation. The remaining C_3 plant fraction is not shown. Panel b) shows the individual C_3 and C_4 $\delta^{13}C_{BB}$ based on plant material $\delta^{13}C_{BB}$ content (green) and direct plume measurements (red), respectively, as well as their weighted averages. The weighted averages based on indirect and direct measurements are –22.2 ± 1.9‰ and –24.7 ± 2.2‰, respectively. While the difference of 2.5‰ between the means is significant, we used the distribution based on the indirect measurements from Cerling *et al*. 1997 [60] in the top-down model due to the larger sample size as described above.

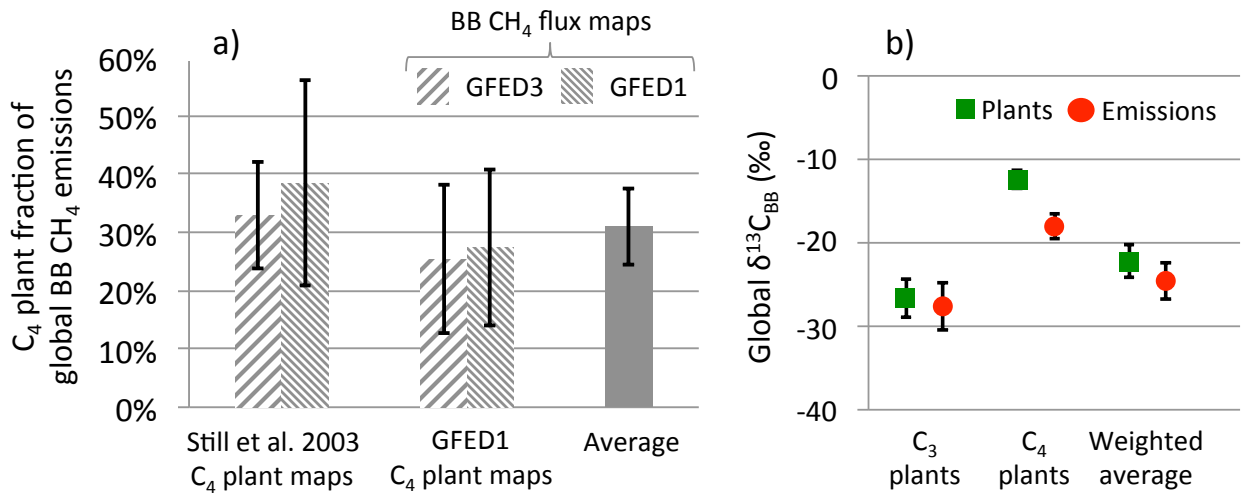

SI Figure 8: Global $\delta^{13}C_{BB}$. Panel a) shows four estimates of the C_4 plant fraction of global BB CH_4 emissions based on two spatial C_4 distribution maps[23,56] and two BB CH_4 flux maps[23]. Solid gray is the mean and 1 SD from a MC simulation assuming all four estimates are equally likely. Panel b) shows C_3 and C_4 $\delta^{13}C_{BB}$ based on plant material $\delta^{13}C_{BB}$ content (green, $N_{C3,C4}$ = 965) in Cerling *et al.* 1997[60], and from a literature review of direct plume measurements (red, N_{C3} = 76, N_{C4} = 6). We attribute the C_4 $\delta^{13}C_{BB}$ difference between plant material data and direct measurements to the small sample size of the latter, and we use the weighted average based on plant material data in our box-model. The weighted averages account for the C_4 plant fraction and uncertainty in panel a).

5. Fossil fuel isotopic signature

A $\delta^{13}C_{Source}$ database[14] of 7,482 $\delta^{13}C_{FF}$ measurements from NG/oil well-heads and coal mines globally was compiled from the peer-reviewed literature, government reports and government databases, and used to estimate a global weighted average $\delta^{13}C_{FF}$. Data are representative of produced natural gas or coal gas from 45 countries which together account for 82% of global natural gas production and 80% of global coal production[16]. Limitations to the database include a lack of natural gas $\delta^{13}C_{FF}$ data from Qatar, Algeria, Malaysia, Turkmenistan, United Arab Emirates and Venezuela, which together account for 12.2% of global natural gas production (2000-2014) and a lack of coal gas $\delta^{13}C_{FF}$ data from India, Indonesia, Kazakhstan, Ukraine and Columbia, which account for 14.5% of global coal production (2000-2014). Other sample biases include over- and under-representation. For example, the two largest gas producers, USA (19.9% of global natural gas production) and Russia (19.4 % of production) comprise 36.6% and 10%, respectively, of the sample count. These biases are mitigated by weighting each country's average $\delta^{13}C_{FF}$ value by its fraction of annual global production, separately for natural gas and

coal (see below). Since data cannot be obtained exhaustively for all producing formations within each country, we assume that the data are broadly representative of the major producing formations and regions. The weighting procedure follows the schematic shown in SI Figure 9, and was implemented in a MC simulation to yield global annual weighted $\delta^{13}C_{FF}$ distributions.

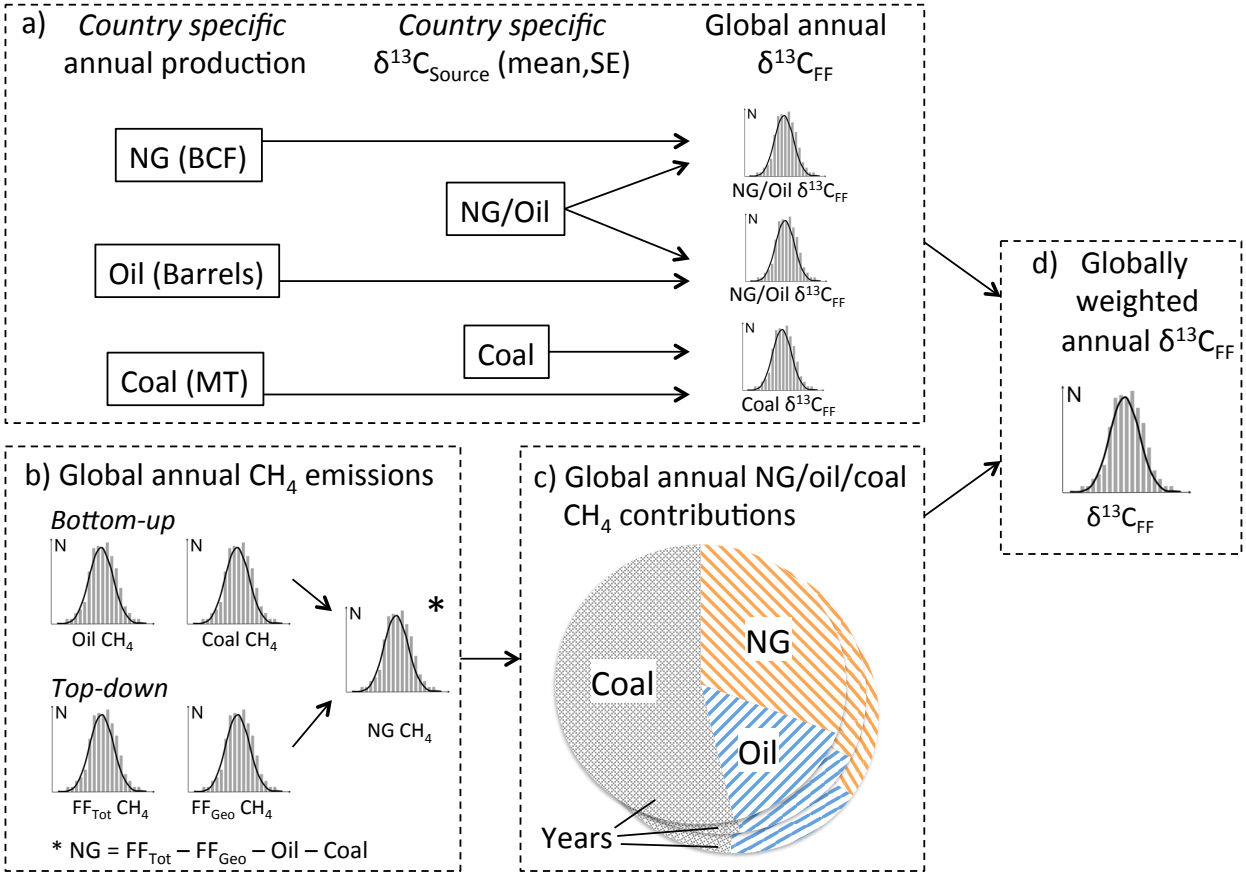

SI Figure 9: Weighting procedure for estimating globally-weighted annual $\delta^{13}C_{FF}$ based on country-specific NG/oil and coal $\delta^{13}C_{FF}$ from our database[14].

Country-specific NG/oil (both are often co-produced) and coal $\delta^{13}C_{FF}$ data were weighted by annual production of NG, oil, and coal. Note that country-level weighting was the smallest feasible geographic scale (as opposed to, e.g., basin-level) due to available $\delta^{13}C_{FF}$ and production data. Given the large sample size and our goal of estimating a global average and its uncertainty (rather than its variability *per se*), country-specific means and the associated standard errors of the mean (SE) were estimated. The resulting global annual NG/oil, and coal $\delta^{13}C_{FF}$ distributions (SI Figure 9, panel a) were weighted by their respective CH_4 contributions (panel c), which

yields global annual weighted $\delta^{13}C_{FF}$ (panel d). Oil and coal CH_4 contributions were determined based on published bottom-up estimates including uncertainties[28]. NG CH_4 emission distributions were estimated as FF_{Tot} (this study) minus FF_{Geo} (this study), oil, and coal (both bottom-up). The weighting in SI Figure 9 was solved iteratively because FF_{Tot} from our top-down model (b) is dependent on the $\delta^{13}C_{FF}$ in (d). Yet, only two iterations were needed given the relatively small differences between the lightest (NG $\delta^{13}C_{FF}$ = –44.5‰) and heaviest sources (coal $\delta^{13}C_{FF}$ = –43.4‰).

The results of steps b) and c) from SI Figure 9 are shown in SI Figure 10, which assumes published[28] bottom-up oil and coal emissions and uncertainties. The large NG emission uncertainties of 51% – propagated from the $\delta^{13}C$ mass balance – are consistent in magnitude with uncertainties (ranging 4–53% with a mean of 25%) from multiple regional and basin-level studies[61]. The IAV in NG CH_4 emissions (panel a) is partly due to model propagation from IAV in global total CH_4 emissions (see SI section 8), and is unlikely to reflect annual changes in NG industry activities. Note also that bottom-up oil and coal emissions assume constant emission factors (EF; largely engineering estimates) over time. Potential emission reductions, particularly for coal, would result in a shallower temporal decline in NG emissions (see main article discussion). Bottom-up uncertainties resulting from ranges in literature EF are described in more detail elsewhere[28]. Panel b) translates the absolute CH_4 emissions from panel a) into relative contributions to total FF_{Ind} CH_4 emissions, which were used to estimate global weighted average $\delta^{13}C_{FF}$.

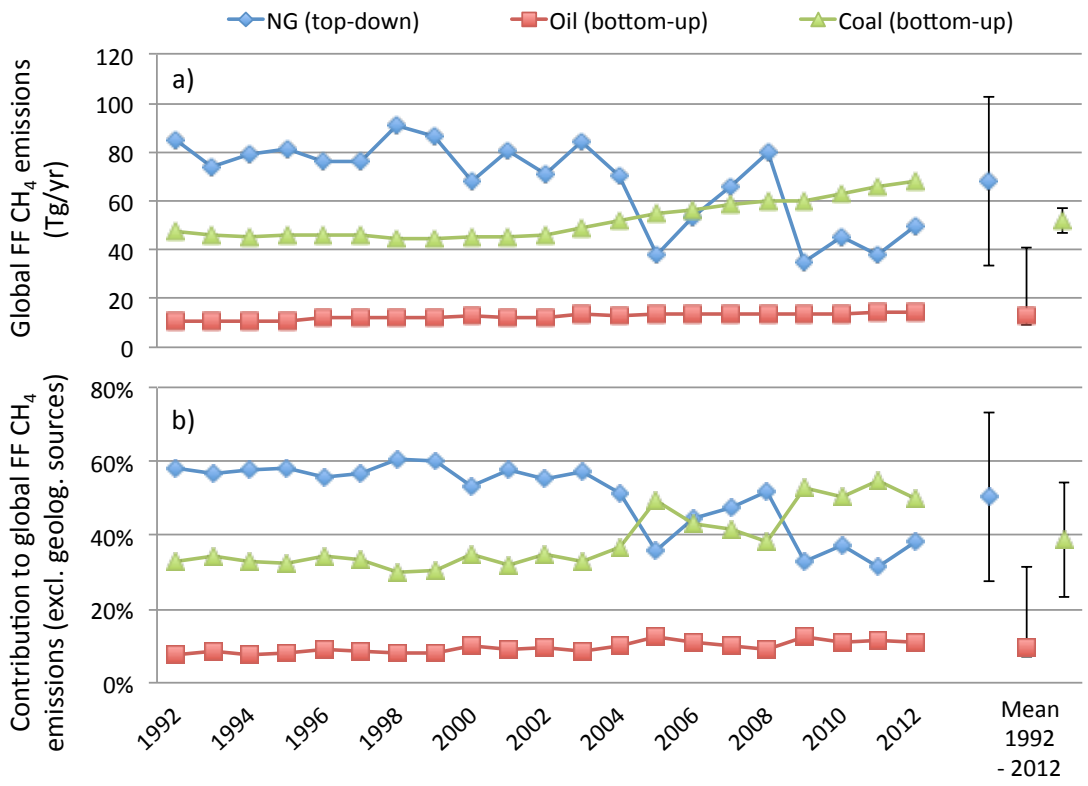

SI Figure 10: Global FF CH_4 emissions by source (panel a) and annual mean contributions of NG, oil, and coal production to global CH_4 emissions (panel b) for estimating weighted average $\delta^{13}C_{FF}$ (see SI Figure 9 b) and c)) for the period during which all country-specific production data for weighting were available. The last column shows averages over 1992-2012 including 1 SD uncertainties (individual year 1 SDs were omitted for legibility, and only negligible variability and trends were observed). Annual values of NG, oil, and coal in panel b) add up to 100%.

The resulting global weighted average $\delta^{13}C_{FF}$ are shown in SI Figure 11. The NG/Oil $\delta^{13}C_{FF}$ weighted by oil production is heavier than weighted by NG production, partly due to proportionally large oil production (as a proxy for emissions) in Saudi Arabia and the U.S. with relatively heavy national average NG $\delta^{13}C_{FF}$ (mean –39.1‰ and –43.1‰, respectively). In contrast, Saudi Arabia's share of global NG production is relatively small, which contributes to a ~0.7‰ lighter global average NG $\delta^{13}C_{FF}$ compared to oil in the 1990s. Note that $\delta^{13}C_{FF}$ in this analysis excludes shale gas methane because the share of these sources to global total NG production increased from only 3% to 9% between 2007 and 2013[16]. Coal $\delta^{13}C_{FF}$ are lighter than oil in most countries because of the influence of microbial methanogenesis in some coal formations[14,19,62]. The ~3.5‰ upward trend in the global coal $\delta^{13}C_{FF}$ is entirely due to China's nearly tripling hard coal production during 1999–2012 (51% of global hard coal production in

2012)[16] and a corresponding Chinese national average coal $\delta^{13}C_{FF}$ of -36.0‰. The ~0.7‰ upward trend in the global NG $\delta^{13}C_{FF}$ during 2002–2012 is mostly due to relative increases in NG production in the U.S. (mean NG $\delta^{13}C_{FF}$ of –43.1‰), Iran (–40.0‰), Saudi Arabia (–40.2‰), Norway (–43.9‰), and China (–41.0‰) as well as relatively decreasing NG production in Canada (–54.7‰). Russia's increase in NG production (–46.4‰) during this period flattens the global NG $\delta^{13}C_{FF}$ trend. Accounting for the relative contributions of NG, oil, and coal to FF_{Tot} emissions (SI Figure 10, panel b), the global weighted average $\delta^{13}C_{FF}$ reflects the upward trend in the NG and coal $\delta^{13}C_{FF}$. The relatively small 1 SDs are the result of the large number of individual $\delta^{13}C_{FF}$ measurements (N = 7,482) in the database.

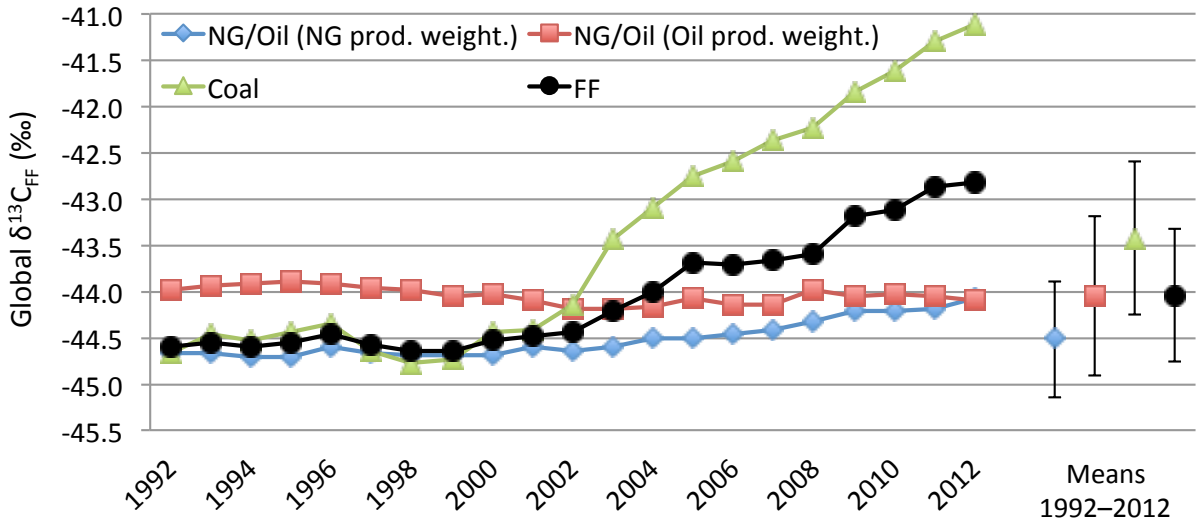

SI Figure 11: Annual global average NG, oil, coal $\delta^{13}C_{FF}$ (all weighted by country-level production) based on the methods described in SI Figure 9 for the period during which all country-specific production data for weighting was available. The last column shows $\delta^{13}C_{FF}$ values averaged over 1992-2012 including 1 SD (individual year 1 SD were omitted for legibility, and only negligible variability and trends were observed).

6. Paleo CH_4 budget and fossil CH_4 emissions from geological seepage

Geological CH_4 sources refer to natural emissions of gas through the Earth's crust in sedimentary, petroleum-prone basins (incl. gas-oil seeps, mud volcanoes, diffuse micro-seepage) and geothermal-volcanic systems[12,63,64]. Bottom-up estimates[12,13,65] of global FF_{Geo} are 45–76 Tg CH_4/yr based on the acquisition of thousands of flux measurements for various seepage types in

12 countries in different petroliferous basins[64]; these were scaled up globally following the concepts of "point sources", "area sources", "activity" and "emission factors" as recommended by EMEP-EEA[66]. In the absence of FF_{Ind} in the pre-industrial era, FF_{Geo} is considered the only source with a $\delta^{13}C_{FF}$ signature. Ice core records of CH_4 levels and $\delta^{13}C$ over the past two millennia[24–26,67] help constrain global FF_{Geo} top-down, but this requires observations about pre-industrial BB emissions, which are not available. Previous studies[24,67] reversed this approach by estimating BB emissions (on average 20-30 Tg CH_4/yr during AD 0–1600) based on outdated bottom-up FF_{Geo} estimates. This range is lower than current day – partly satellite-based – BB estimates of 25-60 Tg CH_4/yr including biofuels and wildfires[11], perhaps due to a smaller human influence in the pre-industrial era. While FF_{Geo} cannot be estimated without assumptions about pre-industrial BB estimates, we verified whether our global $\delta^{13}C_{Source}$ inventory is consistent with previous FF_{Geo} estimates and the above model-derived pre-industrial BB emissions. Note that we assume that the temporal average $\delta^{13}C_{FF}$ based on NG/oil well and coal mine data is representative of FF_{Geo} CH_4 emissions. Since there is no significant isotopic fractionation during gas migration in petroleum systems from reservoir to the surface[68,69] (although molecular fractionation does occur[68,69]), potential differences in $\delta^{13}C_{FF}$ between CH_4 emissions from FF_{Ind} and FF_{Geo} may only result from a potential sampling bias in our (however large) $\delta^{13}C_{FF}$ database, i.e., reservoir depths (largely determining reservoir pressure and thus the level of thermogenic methane formation and $\delta^{13}C_{FF}$) of the samples vs. the seepage source. Yet, even a large hypothetical difference of 5‰ between $\delta^{13}C_{FF}$ from FF_{Ind} and FF_{Geo} would change FF_{Geo} CH_4 emissions by only ~20% (well within uncertainties) in our model described below.

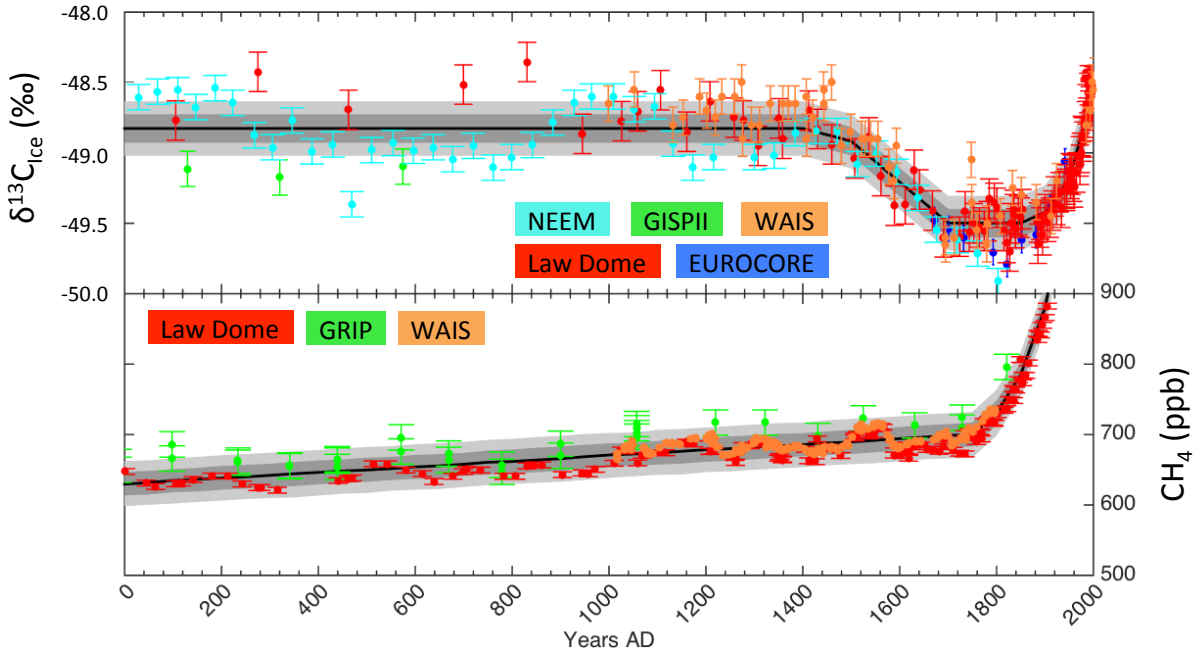

SI Figure 12: Ice core records of CH_4[24–26,67] mixing ratios and $\delta^{13}C$ over the past two millennia shown as colored dots (reproduced from Sapart *et al.* 2012[24]), which informed the distributions (light and dark gray represent 10th/90th and 25th/75th percentiles, respectively) used in the box-model.

We estimated FF_{Geo} emissions analogously to Equations 1-11, but $X_{CH4,t}$ and $\delta^{13}C_{Atm,t}$ were replaced with $X_{CH4,Ice,t}$ and $\delta^{13}C_{Ice,t}$ using literature[24–26,67] data shown in SI Figure 12. This method is similar to previous analyses[24,67], but it varies in two ways. First, we used updated $\delta^{13}C_{Source}$ from our global inventory described above (e.g., lighter $\delta^{13}C_{FF}$), which influence the derived emission attribution between geological, BB, and microbial sources. Second, we simplify the analysis by focusing only on multi-centennial-scale trends in the measurements because centennial-scale variations are unlikely caused by changes in geological CH_4, which is in agreement with previous studies[24,67]. Original data from different sources in SI Figure 12 (colored circles with error bars) are plotted as a reference, which show a $\delta^{13}C_{Ice}$ decrease during ~1400–1800 followed by an increase until 2000 as well as a steady increase in CH_4 during ~0–1750 followed by a more rapid increase thereafter. These major trends are accounted for in the box-model as shown by the shaded areas. Pre-industrial BB emissions of 20-30 Tg CH_4/yr during AD 0–1600 were prescribed consistent with the literature [24,67] (including a gradual decline by 10 Tg CH_4/yr in 1800 followed by a gradual increase of 15 Tg CH_4/yr in 2000). We assumed the same OH and soil sink ranges as in current decades (SI Table 1) consistent with previous studies[24,67]. This results in

FF_{Geo} emissions of 22–78 Tg CH_4/yr (10^{th}/90^{th} percentiles) with a mean of 51 Tg CH_4/yr (averaged over AD 0–1700) as shown in SI Figure 13.

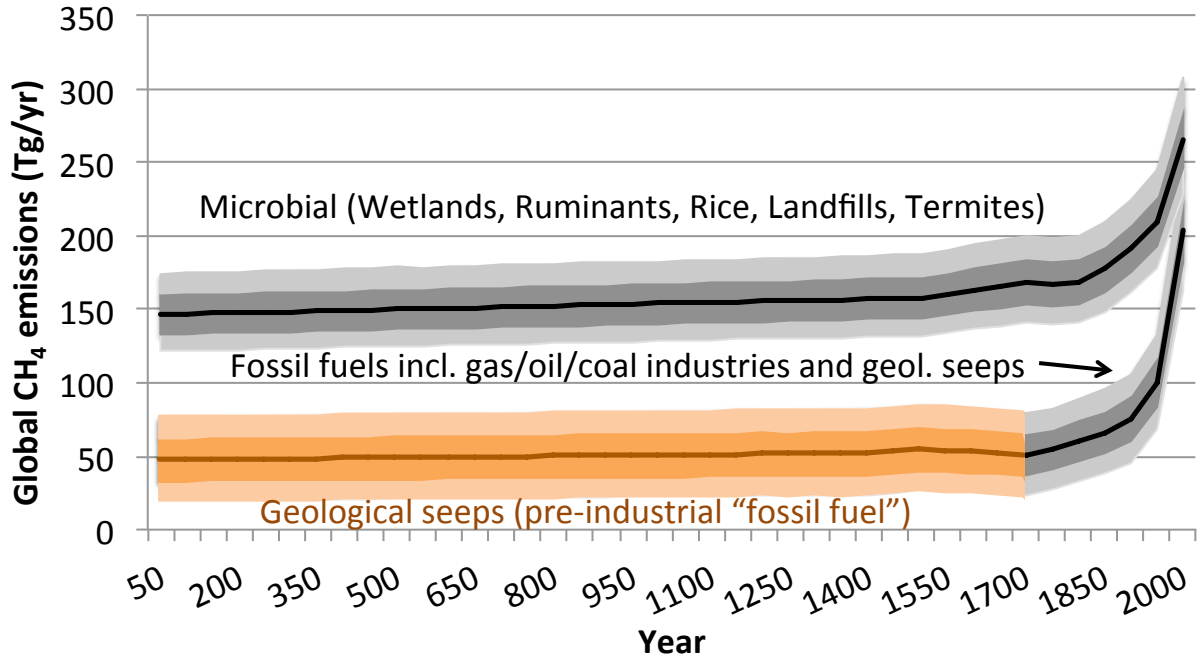

SI Figure 13: Box-model results using literature ice core records of CH_4 and $\delta^{13}C$ (SI Figure 12), and prescribed BB emissions (see text). The light and dark bands represent the 10^{th}/90^{th} and 25^{th}/75^{th} percentiles, respectively. Orange marks the FF_{Geo} portion of FF_{Tot}.

Our FF_{Geo} range is consistent with the bottom-up range of 45–76 Tg CH_4/yr[13,65], and the top-down radiocarbon-based range of 42–64 Tg CH_4/yr[12]. Our mean value is similar to the 44 Tg CH_4/yr prescribed geological emissions in Sapart *et al.*[24] because of an offsetting effect of differences in isotopic signatures (our $\delta^{13}C_{Mic}$ and $\delta^{13}C_{FF}$ are 2‰ and 6‰ lighter, respectively) and isotopic fractionation factor (our ε range of -5.5‰ to -7.1‰ compared to -5.4‰). Ferretti et al.[67] use an ε of -7.4‰, i.e., our ε range roughly spans the values used in Sapart *et al.*[24] and Ferretti et al.[67], and the seepage estimate in the latter is only 12 Tg CH_4/yr because of relatively heavy $\delta^{13}C_{Mic}$ and $\delta^{13}C_{FF}$ values of -60.0‰ and -40.0‰, respectively. We conclude that our distribution of geological CH_4 emissions is consistent with literature estimates over a range of parameter choices.

The previous inverse-based CH_4 microbial source mean estimate of 440 Tg CH_4/yr (b) compared to the 160 Tg CH_4/yr in the paleo-record (SI Figure 13) may be explained by increased Ag/Waste/LF emissions due to population growth. However, this 280 Tg CH_4/yr modern–paleo

difference is significantly larger than the 90–140 Tg CH_4/yr from modern total Ag/Waste/LF (our most likely scenarios S2 and S5; SI Figure 14). This study's downward revision of the microbial source (and the resulting modern–paleo difference of only 180 Tg CH_4/yr) provides a more consistent explanation assuming that natural microbial sources (mainly wetlands) have not doubled (b and SI Figure 5) between paleo and modern times.

7. Global TM5 simulations

The broad spatial distribution of some CH_4 source categories is relatively well known. For example, ~ 92% of FF_{Tot} CH_4 is emitted in the Northern Hemisphere[2] with smaller values for agriculture (including livestock and rice production), waste, landfills (Ag/Waste/LF) at 82%[2] and natural wetlands at 54%[70,71]. By simulating global atmospheric CH_4 mole fractions using emissions maps scaled by select CH_4 source attribution scenarios using the global atmospheric chemistry and transport model TM5[27] and comparing the resulting CH_4 levels across latitudes with observations[20] we included a spatial constraint in our analysis in addition to the mass balance.

Data sources for generating CH_4 source attribution scenarios and grid maps

SI Table 2 provides a summary of the data sources used in generating CH_4 source attribution scenarios including simulated total CH_4 emissions, spatial flux distribution, and seasonal cycles for each source category. The total emissions column describes the data sources that informed the magnitude of the grid map scaling as described in more detail below. Fluxes were input to TM5 at 1° x 1° resolution, and existing grid maps with higher resolution were adjusted accordingly.

SI Table 2: Data sources for spatial emission distributions (grid maps) and scaling of grid maps used to generate emission attribution scenarios for TM5 simulations.

	Total emissions	Spatial distribution	Seasonal cycle
Fossil Fuels (FF_{Tot})	Box model (BM)	EDGAR4.2[2]	n/a
Natural (wetlands, termites, wild animals, soil sink,	Bergamaschi (2007)[72] (scenarios 1, 4, 6); other scenarios see text	Fung (1987)[70] and Kaplan (2002)[71]; [a]	Bergamaschi (2007)[72]; [b]
Biomass burning	Schultz (2008)[73] (1980-1996), Giglio (2006)[59] and Van Der Werf (2006)[74] (1997-2012)	Schultz (2008)[73] (1980-1996), GFED (2013)[75] (1997-2012)	
Agriculture/waste/landfill (incl. agric. waste burning)	BM global budget minus sum of all other sources; global trend attributed fully to Ag/Waste/LG	EDGAR4.2[2]	Matthews (1991)[76]; [c]

Notes: [a] Natural source grid maps in scenarios S1, S4, and S6 (see SI Figure 14) are unmodified, but the wetlands fractions were scaled up between 0°N and 25°S in scenarios S2/S5/S8 (51 Tg CH_4/yr each) and in scenarios S3/S9 (102 Tg CH_4/yr each). [b] Seasonal cycle included for wetlands. [c] Seasonal cycle included for rice cultivation.

Description of simulated CH_4 source attribution scenarios

The simulated emission scenarios are summarized in SI Figure 14. Total CH_4 emissions from all sources (excluding soil sink) equal the total CH_4 emissions from the box model to allow direct comparison of TM5 results and the box model. The scenarios assume the mean box model CH_4 lifetime of 9.0 years, and the TM5 OH field was scaled (uniformly across space) such that global chemical destruction is approximately equivalent to the box model CH_4 lifetime. We simulated three FF scenarios that encompass approximately the 10^{th}/90^{th} percentile range in the box model (150, 200, and 250 Tg CH_4/yr). This range includes FF_{Ind} and FF_{Geo}, and measurements[65] suggest that both sources are generally co-located. The same BB grid maps and absolute CH_4 emissions were used in each scenario. Scenarios S1, S4, S6, and S7 include 175 Tg CH_4/yr natural emissions from Bergamaschi et al. (2007)[72] (consistent with the mean of several other top-down studies[3,6,7]). The simulated natural emissions also include a residual IAV component after accounting for IAV from BB and global total CH_4 emissions based on the assumption that anthropogenic source IAV is very small compared to natural source IAV. We attributed the remainder of the global CH_4 budget including its 25 Tg growth over time to the Ag/Waste/LF source. The box model CH_4 growth allocation is more complex as described above (~45 Tg increase from either natural or Ag/Waste/LF, and a FF decrease of ~20 Tg, all after 2004).

However, these details were disregarded for simplicity and because such small budget terms are likely to have only a minor affect on the simulated N–S gradient, which is the focus of the TM5 modeling. Scenarios S2, S3, S5, S8, and S9 explore the hypothesis of underestimated tropical wetland emissions by up-scaling this source between the equator and 25°S by 51 or 102 Tg CH_4/yr, and down-scaling the Ag/Waste/LF grid maps uniformly by 50 or 100 Tg CH_4/yr. We introduced the 1 and 2 Tg CH_4/yr differences between up-scaling natural emissions and down-scaling Ag/Waste/LF emissions to partly account for the larger OH sink in the tropics and rapid vertical distribution of emissions relative to mid-latitudes (see description below).

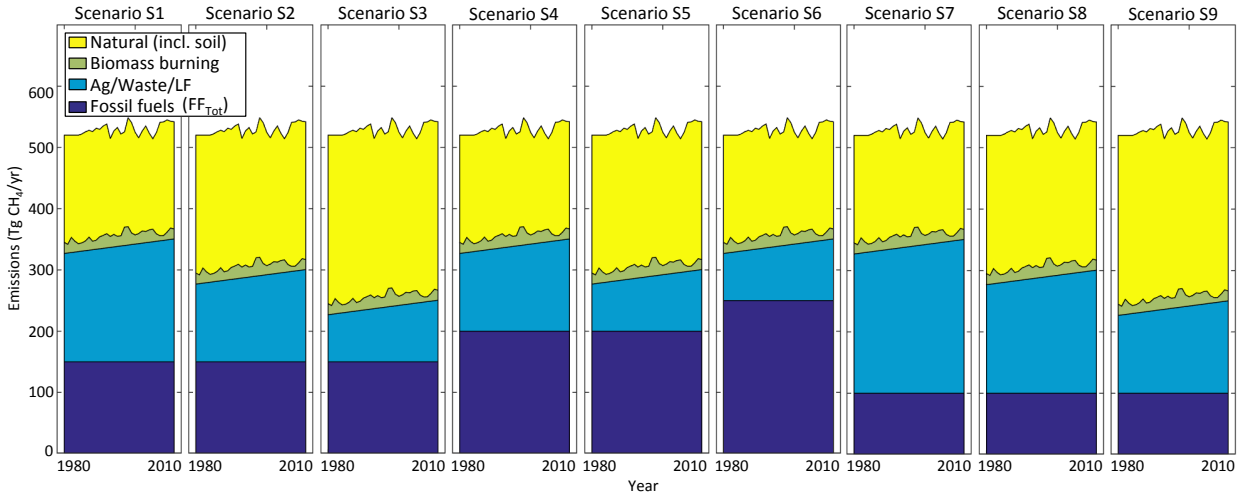

SI Figure 14: Total CH_4 emissions of individual source categories in each scenario simulated using the TM5 model. The data sources underlying each scenario are described in SI Table 2. Note that the total CH_4 emissions from all sources (excluding soil sink) equal the total CH_4 emissions from the box model based on annual mean, globally averaged CH_4 levels and mean CH_4 lifetime (SI Figure 2).

Simulated and observed latitudinal CH_4 gradients

The simulated and observed N–S gradients are illustrated in SI Figure 15a-c for 2010 (see other years in SI Figure 16), and all scenarios are consistent with the $\delta^{13}C$ mass balance (including FF_{Tot} ranging from 150–250 Tg/yr). Scenario S6 (250 Tg CH_4/yr FF_{Tot}) results in the largest gradient overestimation relative to observations (~40 ppb; SI Figure 15b) indicating inconsistency between the $\delta^{13}C$ mass balance 90th percentile and the observed N–S gradient. Scenario S3 explores low FF_{Tot} emissions (150 Tg CH_4/yr, i.e. $\delta^{13}C$ mass balance 10th percentile) combined with substituting 100 Tg CH_4/yr from Ag/Waste/LF for tropical natural emissions, which leads to the largest N–S gradient underestimation (~35 ppb). The N–S gradient

discrepancy is reduced more effectively by a combination of substituting Ag/Waste/LF with tropical natural emissions and reducing the FF_{Tot} component (S6→S5) than by reducing FF_{Tot} alone (S6→S1). Previous 3D inversions also found that overestimated *a priori* high latitude sources needed to be compensated by increases at lower latitudes[4,77], particularly tropical wetlands[4]. Overall, scenarios S2 and S5 (150 and 200 Tg CH_4/yr FF_{Tot}, respectively) are (i) the spatially most consistent with observations, and (ii) consistent with the $\delta^{13}C$ mass balance.

Scenarios S7–S9 include only 100 Tg CH_4/yr FF_{Tot}, which is representative of the literature[3–8], yet inconsistent with the $\delta^{13}C$ mass balance. We find that S7–S9 are also inconsistent with the observed N–S gradient (especially in comparison with S2 and S5, considering that all scenarios are subject to the same model uncertainties including simulated transport and spatially modeled OH field). Scenarios S7–S9 do not match observations as well as S2 and S5 in the Southern and/or Northern Hemispheres. Note that we used the recently updated version of the TM5 global chemical transport model, which has improved vertical mixing relative to the parent model[78].

The atmospheric CH_4 levels of some scenarios are lower than observations in both hemispheres (SI Figure 15b) due to a model artifact, which has only a minor effect on the N–S gradient interpretation (see detailed description below). Also, the consistent overestimation of CH_4 levels between 6–17°N (0.1–0.3 sine(latitude) in SI Figure 15b) may be reduced by improving the emission grid spatial/source allocation within the tropics, but this is beyond the scope of this analysis. For instance, Saunois *et al*. (2016)[79] highlight that wetland extent dominates the uncertainty of modeled CH_4 emissions from wetlands (the largest single source in the tropics).

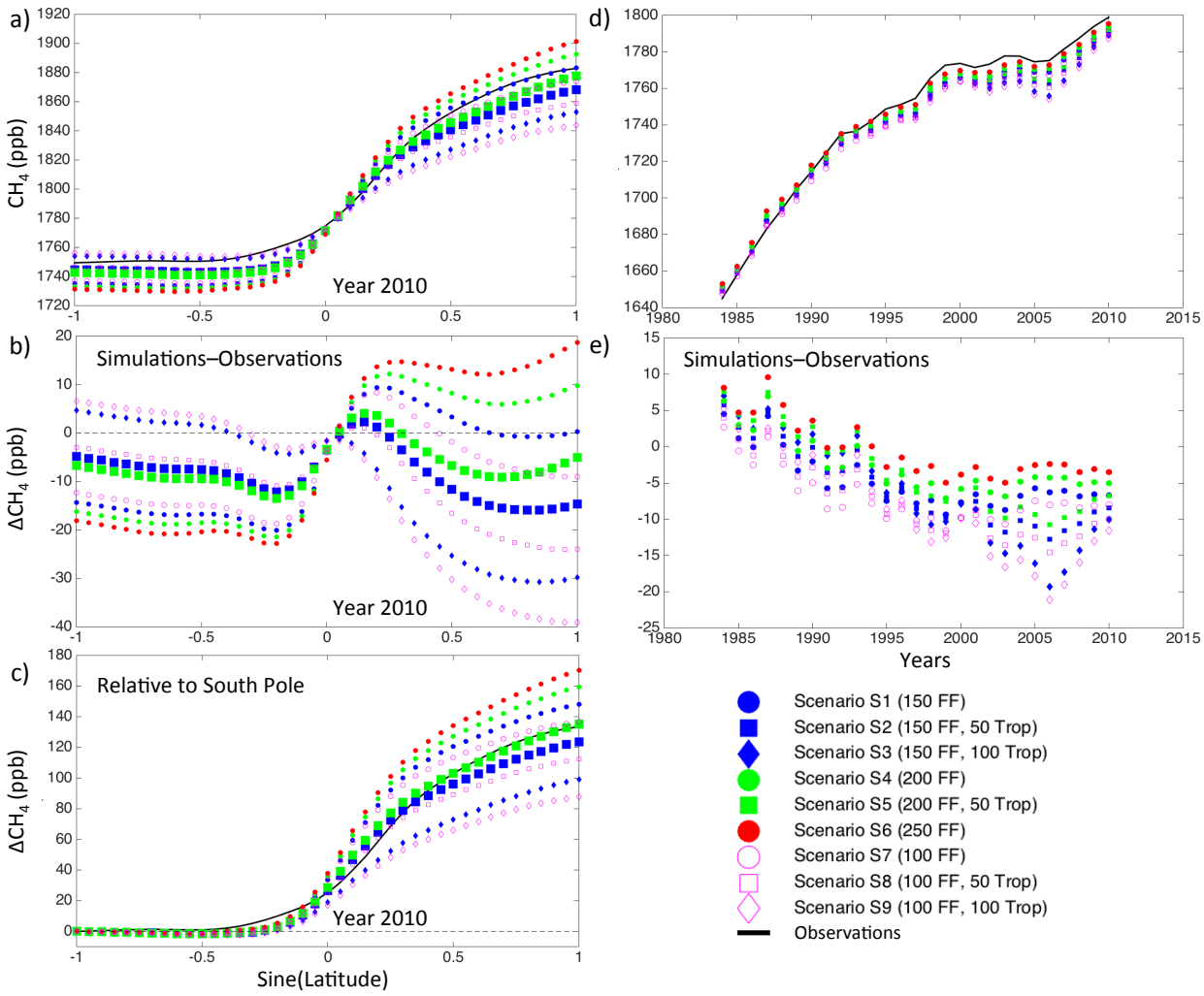

SI Figure 15: TM5 forward simulation results for nine emission scenarios and NOAA measurements[20]. (a) Annual mean CH_4 dry air mole fractions across 41 latitudinal bands in 2010 (see SI Figure 16 for additional years). (b) Simulations minus observations. (c) Simulations and measurements relative to South Pole (sine(latitude) = -1). (d) Annual mean, globally averaged CH_4 dry air mole fractions; see SI section 2 for Marine Boundary Layer sites and references[45,46] for estimating global averages from spatial distributions.

Global total CH_4 level differences between observations and simulations (model artifact)

The simulated and observed annual mean, globally averaged CH_4 levels for all years are shown in SI Figure 15 (panels d, e). The simulated CH_4 of all scenarios generally follows the observed trend as expected because simulated annual total CH_4 emissions were scaled according to observed global means using the box-model (SI section 1). Note that scenario-dependent amounts of CH_4 (spatially varying emissions among scenarios) are consumed in the 3D model

because (i) the OH sink is larger in the tropics than in lower latitudes (more water vapor, higher temperatures, and more solar radiation), and (ii) emissions are distributed through a deeper atmospheric column. However, the empirical tuning of the total OH sink in TM5 was applied only once for all scenarios. In contrast, the box-model considers a global average CH_4 sink. Thus, some simulation–observation mismatches are expected because relatively high tropical emissions in some scenarios, e.g. S3 vs. S1, lead to greater total CH_4 destruction, thus lower global average CH_4 levels. The particular simulation–observation mismatches in SI Figure 15 (panels d, e) are explained as follows. (i) The constant simulated emissions during 1980-1983 (for model initialization; SI Figure 14) are likely too high in absence of observations, which results in overestimated CH_4 levels. (ii) This surplus CH_4 decreases over time as "true" emissions increase to the simulated values, and the surplus has decayed by the early-1990s (approximately one CH_4 lifetime after 1983). (iii) Simulations and observations are roughly in balance starting in 1994 for scenarios without added tropical emissions (S1/4/6/7). (iv) In 2000/2001 and 2004/2005 total global emissions drop by ~20 Tg/yr, but scenarios S2/3/5/8/9 include a fixed shift of emissions (50 or 100 Tg/yr) from Northern mid-latitudes to the tropics (where CH_4 destruction is greater). This increases global total CH_4 destruction relative to S1/4/6/7 and observations, which leads to lower global CH_4 levels relative to S1/4/6/7 and observations until the pre-2001 simulations–observations difference is achieved again. Note, however, that while this model artifact influences simulated global average CH_4 levels, it has little bearing on the simulated N–S gradients given the relatively fast inter-hemispheric atmospheric mixing of ~1 year.

Simulated and observed latitudinal CH_4 gradients (additional years)

SI Figure 16 shows the N–S gradient (simulations minus observations for 5-year intervals between 1985 and 2010 for comparison with SI Figure 15b. The general patterns and differences among the scenarios are qualitatively similar, and do not alter the conclusions drawn based only on 2010 in the main article. Note that 1985 represents CH_4 levels only 5 years after the initialization and start of the simulation, thus relatively large differences compared to later years are expected.

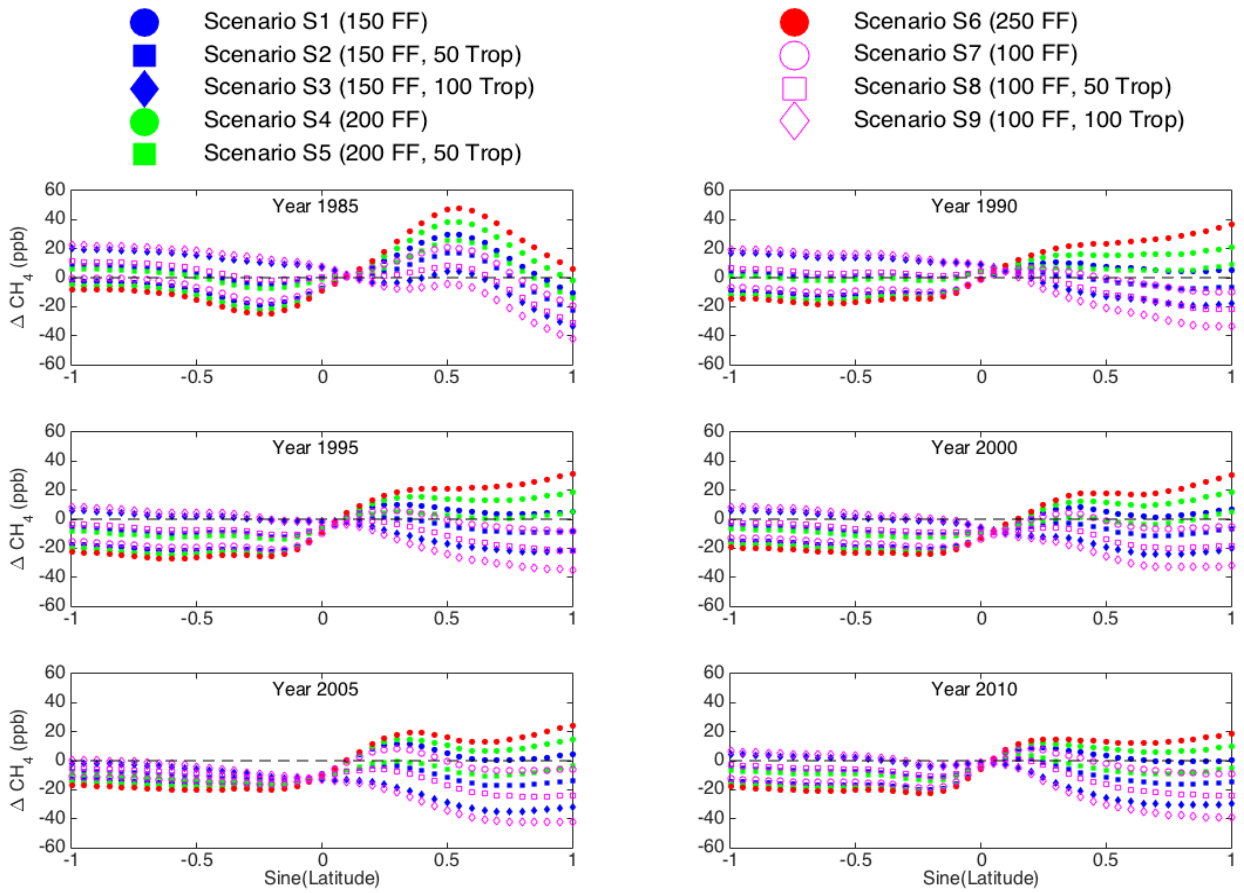

SI Figure 16: Differences between annual mean simulated CH_4 mixing ratios across 41 latitudinal bands between 1985 and 2010 and NOAA's measurements.

8. Sensitivity analysis and additional information

The sensitivity analysis identifies the uncertain parameters with the largest influence on total FF CH_4 emissions $Q_{FF,Tot,t}$ and FER, which is summarized in SI Figure 17 for 2013 (other years are qualitatively the same, but not displayed). The "tornado" diagram shows the changes in $Q_{FF,Tot,t}$ (panel a) and FER (panel b) after varying one input parameter at a time within their respective 10^{th}/90^{th} percentiles from SI Table 1. For instance, varying these input parameters one at a time changes global FF_{Tot} up to ±25 Tg/yr and FER up to ±1.0 percentage point. It shows that $Q_{FF,Tot,t}$ and FER are most sensitive to BB CH_4 emissions Q_{BB} and the isotopic fractionation factor ε, whose model input distributions are relatively wide. Keeping all other parameters at their mean values, $Q_{FF,Tot,t}$ and FER could range from 166–215 Tg CH_4/yr and 1.2–3.3% for Q_{BB} of 31–55 Tg CH_4/yr, respectively. The isotopic signature of the microbial source $\delta^{13}C_{Mic}$ is the third most sensitive parameter despite its relatively narrow distribution range of approximately ±1‰, illustrating the importance of empirical $\delta^{13}C_{Mic}$ data. Panels c) and d) illustrate the sensitivities of

potential trends of individual parameters during 1985–2013 on the trends of $Q_{FF,Tot,t}$ and FER. The Q_{BB} trends investigate a hypothetical gradual trend of 20% of model mean Q_{BB} (8 Tg CH_4, which is also the 1 SD inter-annual variability[74] of Q_{BB}). Note that observed global fire emissions[74] do not indicate a trend, but this may not fully account for CH_4 emissions from fuel biomass burning. The Q_{BB} trends are illustrated for scenarios in which the entire Q_{BB} trend is allocated to either C_4 or C_3 plants. If the Q_{BB} had increased from 39 Tg CH_4/yr in 1985 to 47 Tg CH_4/yr in 2013, the mass balance would require global total FF CH_4 emission reductions of 15–22 Tg CH_4/yr during this period. The $\delta^{13}C_{Mic}$ trend sensitivities assume the 30 Tg CH_4 trend from Figure 2a allocated to either wetlands or Ag/Waste/LF.

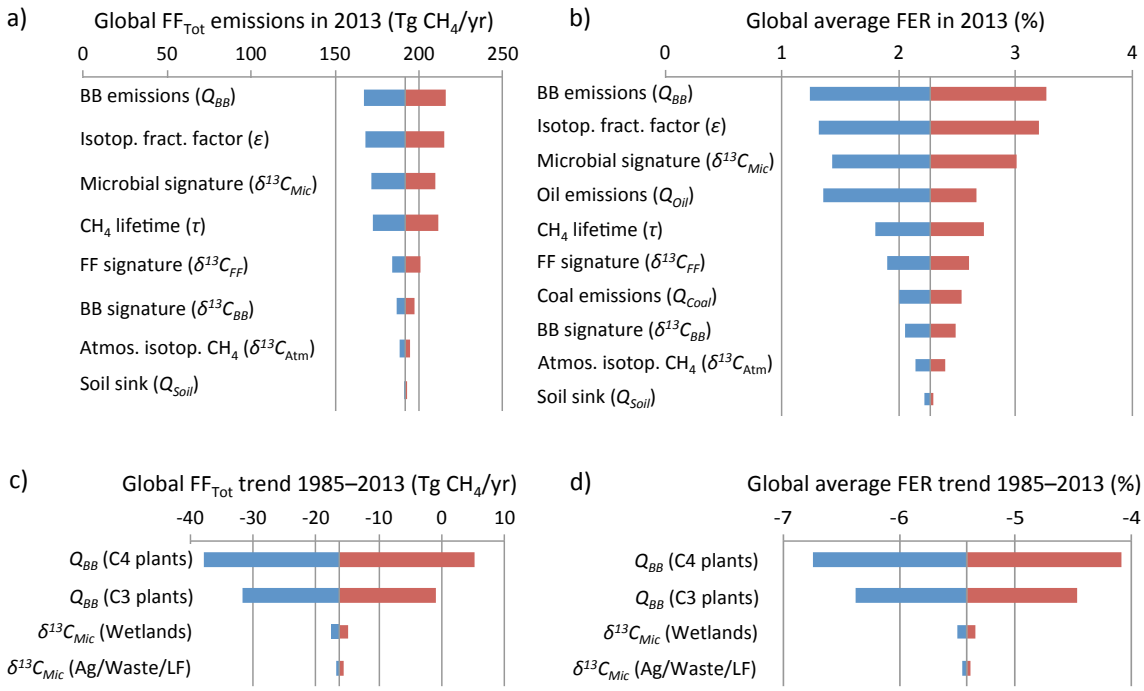

SI Figure 17: Tornado diagram illustrating the sensitivity of total FF CH_4 emissions (a) and global average FER (b) to individual parameters in 2013, and the sensitivities of the trend of FF CH_4 emissions (c) and global average FER (d) to individual parameters during 1985–2013. The ordinates in a) and b) are centered at model mean values and the red and blue bars show the values of the dependent variables after changing one parameter at a time to its 10th and 90th percentile value (see SI Table 1), respectively. The variable $\delta^{13}C_{Atm}$ pertains to the 0.1‰ uncertainty in the global average atmospheric isotopic value (SI section 2). The trend sensitivities are centered around the mean trends shown in Figures 2a and 3 (main article), which account for the $\delta^{13}C_{FF}$ trend in SI Figure 11. There is no total FF CH_4 emissions trend when assuming temporally constant $\delta^{13}C_{FF}$ (see blue lines in Figure 2a). There is a –6.4% FER trend when assuming temporally constant $\delta^{13}C_{FF}$ (not shown; see blue lines in Figure 3). The BB emission trend sensitivities assume a gradual 20% BB emission trend (see text) allocated to either C_4 or C_3 plants. The $\delta^{13}C_{Mic}$ trend sensitivities assume the 30 Tg CH_4 trend from Figure 2a allocated to either wetlands or Ag/Waste/LF.

The original box-model results including IAV are shown in SI Figure 18. The IAV is partly an artifact of multiple components that our model does not control including CH_4 sink IAV and the $\delta^{13}C_{BB}$ IAV depending on the dominating BB type (C_3 vs. C_4) in a given year. For example, a temporal sink increase in areas of predominantly microbial sources (e.g. Tropics) could increase the global average $\delta^{13}C_{Atm}$ to suggest – via mass balance – an increase in isotopically heavier sources such as FF. Considering the average global mean OH sink variability of ~2% or ~10 Tg CH_4/yr (ref[37]), CH_4 sink IAV can explain a significant fraction of the source allocation IAV and FER IAV as a model artifact in SI Figure 18.

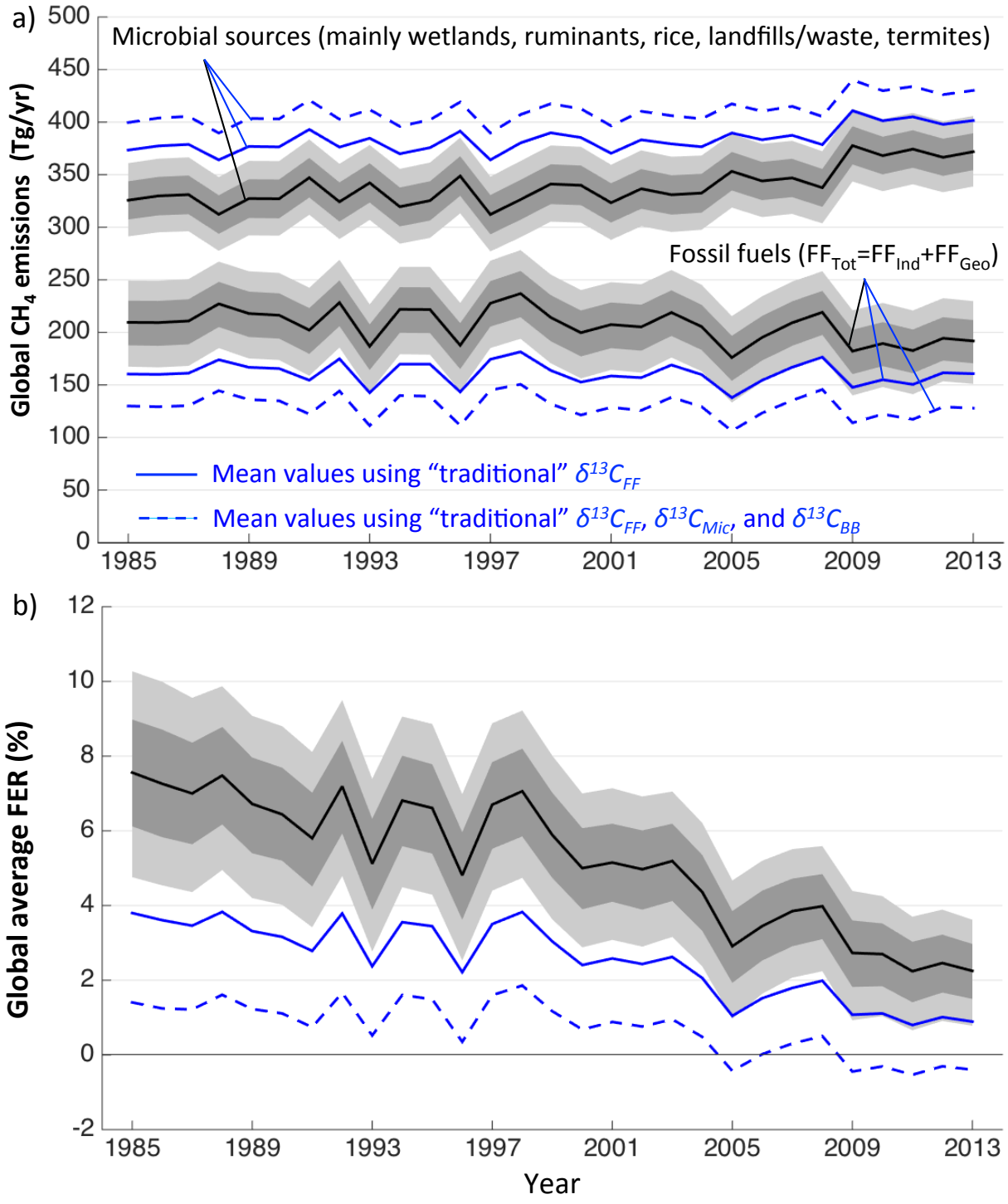

SI Figure 18: Unfitted long-term trends in global microbial and total FF_{Tot} CH_4 emissions (a) and global average FER (b) as shown in Figures 2a and 3 (main article), but including IAV. The magnitude of IAV is partly an artifact of multiple components not accounted for in this model (see text).

To achieve more accurate FER estimates, and to further reduce FER uncertainty, future work may further investigate these parameters. Parameters $Q_{FF,Tot,t}$ and FER are less sensitive to $\delta^{13}C_{FF}$ relative to $\delta^{13}C_{Mic}$, partly due to a narrower input distribution range.

The review of $\delta^{13}C_{Source}$ used in the top-down literature and summarized in FF is based on the following list of references (not included in the main text due to reference count limits): Stevens *et al*. (1988)[80], Craig *et al*. (1988)[81], Whiticar *et al*. (1990)[17], Whiticar *et al*. (1993)[82], Levin *et al*. (1994)[83], Gupta *et al*. (1996)[84], Tyler *et al*. (1999)[85], Quay *et al*. (1999)[10], Houweling *et al*. (2000)[86], Mikaloff *et al*. (2004)[4], Bousquet *et al*. (2006)[3], Lassey *et al*. (2007)[87], Neef *et al*. (2010)[88], Dlugokencky *et al*. (2011)[89], and Monteil *et al*. (2011)[90]. SI Figure 19 shows the literature mean budget term values as a close-up from Figure 2b (main article).

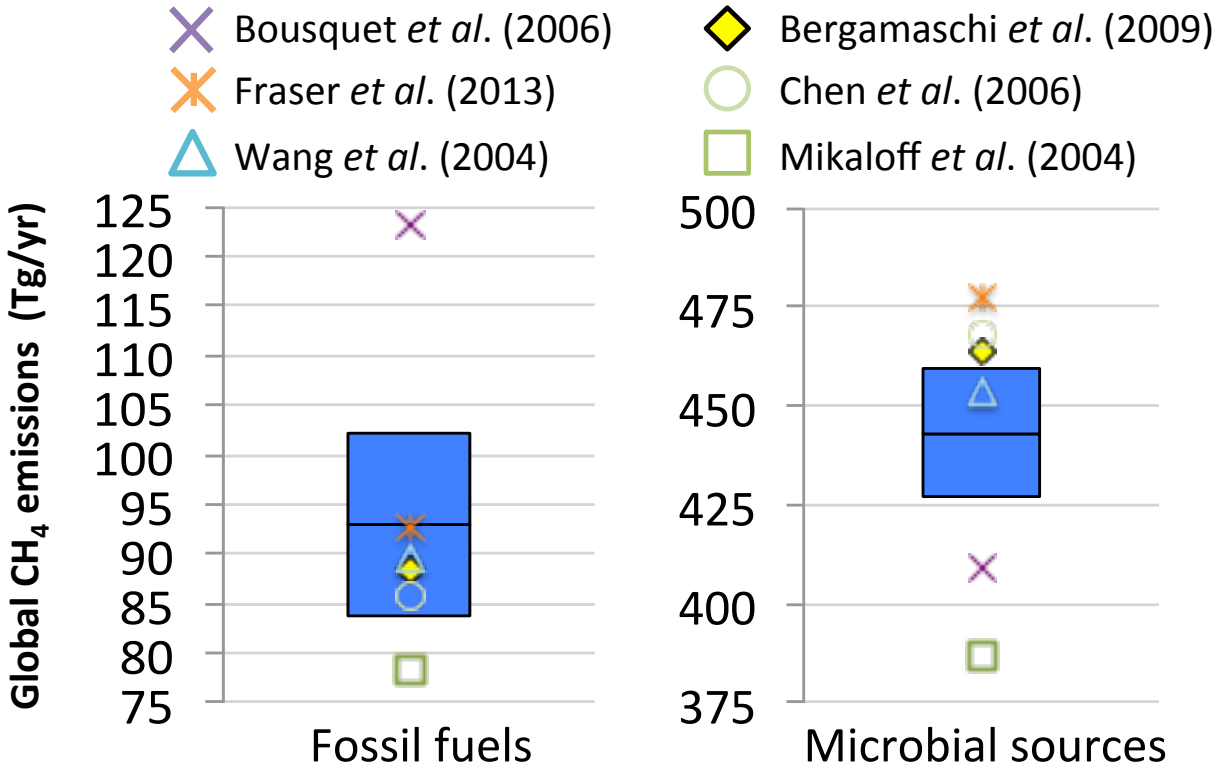

SI Figure 19: Close-up of literature columns in FFb (main article). Note that the literature[3–8] budget terms were scaled to match the mean total CH_4 budget in this study. Literature 1 SD uncertainties are 9 Tg CH_4/yr on average.

References

31. Fung, I., Prather, M., John, J., Lerner, J. & Matthews, E. Three-dimensional model synthesis of the global methane cycle. *J. Geophys. Res.* **96,** 13033–13065 (1991).

32. Prather, M. J., Holmes, C. D. & Hsu, J. Reactive greenhouse gas scenarios: Systematic exploration of uncertainties and the role of atmospheric chemistry. *Geophys. Res. Lett.* **39,** (2012).

33. Voulgarakis, A. *et al*. Analysis of present day and future OH and methane lifetime in the ACCMIP simulations. *Atmos. Chem. Phys.* **13,** 2563–2587 (2013).

34. Prinn, R. G., Huang, J., Weiss, R. F. & Cunnold, D. M. Evidence for variability of atmospheric hydroxyl radicals over the past quarter century. *Geophys. Res. Lett.* **32,** 2–5 (2005).

35. Naik, V. *et al*. Preindustrial to present-day changes in tropospheric hydroxyl radical and methane lifetime from the Atmospheric Chemistry and Climate Model Intercomparison Project (ACCMIP). *Atmos. Chem. Phys.* **13,** 5277–5298 (2013).

36. Montzka, S. A. *et al*. New Observational Constraints for Atmospheric Hydroxyl on Global and Hemispheric Scales. *Science (80-.).* **288,** 500–503 (2000).

37. Montzka, S. A. *et al*. Small interannual variability of global atmospheric hydroxyl. *Science* **331,** 67–69 (2011).

38. Hartmann, D. L. *et al*. in *Climate Change 2013: The Physical Science Basis. Contribution of Working Group I to the Fifth Assessment Report of the Intergovernmental Panel on Climate Change* (eds. Stocker, T. F. et al.) **AR5,** (Cambridge University Press, 2014).

39. Lassey, K. R., Lowe, D. C. & Manning, M. R. The Trend in Atmospheric Methane Delta C-13 Implications for Isotopic Constraints on the Global Methane Budget. *Global Biogeochem. Cycles* **14,** 41–49 (2000).

40. Miller, J. B. in *Stable isotopes and biosphere-atmosphere interactions* (eds. Flanagan, L. B., Ehleringer, J. R. & Pataki, D. E.) 288–310 (Elsevier, 2005).

41. Tans, P. P., Berry, J. A. & Keeling, R. F. Oceanic 13 C/ 12 C observations: A new window on ocean CO 2 uptake. *Global Biogeochem. Cycles* **7,** 353–368 (1993).

42. Gröning, M. in *Handbook of Stable Isotope Analytical Techniques* (ed. de Groot, P. A.) 874–906 (2004).

43. NOAA Global Monitoring Division. Current trends in CH4. (2016). Available at: http://www.esrl.noaa.gov/gmd/ccgg/trends_ch4/.

44. NOAA Global Monitoring Division. NOAA Greenhouse Gas Marine Boundary Layer Reference. (2016). Available at: http://www.esrl.noaa.gov/gmd/ccgg/mbl/mbl.html.

45. Masarie, K. A. & Tans, P. P. Extension and integration of atmospheric carbon dioxide data into a globally consistent measurement record. *Journal of Geophysical Research* **100,** 11593 (1995).

46. Dlugokencky, E. J., Steele, L. P., Lang, P. M. & Masarie, K. A. Atmospheric methane at Mauna Loa and Barrow observatories: Presentation and analysis of in situ measurements. *Journal of Geophysical Research* **100,** 23103 (1995).

47. Miller, J. B. *et al*. Development of analytical methods and measurements of 13C/12C in atmospheric CH4 from the NOAA Climate Monitoring and Diagnostics Laboratory Global Air Sampling Network. *J. Geophys. Res. Atmos.* **107,** ACH 11–1–ACH 11–15 (2002).

48. Levin, I. *et al*. No inter-hemispheric δ13CH4 trend observed. *Nature* **486,** E3–E4 (2012).

49. Englund Michel, S. *Personal communication*. (2016).

50. Food and Agriculture Organization of the United States. *Live Animal Stocks Statistics*. *http://faostat3.fao.org/browse/Q/QA/E*. (2015).

51. USDA Economic Research Service. *Feed Grains: Yearbook Tables*. *http://www.ers.usda.gov/data-products/feed-grains-database/feed-grains-yearbook-tables.aspx#26941*. (2015).

52. Vasconcelos, J. T. & Galyean, M. L. Nutritional recommendations of feedlot consulting nutritionists: The 2007 Texas Tech University survey. *J. Anim. Sci.* **85,** 2772–2781 (2007).

53. U.S. Department of Agriculture (USDA) / Animal and Plant Health Inspection Service (APHIS). *Beef Cow/Calf Health and Productivity Audit. PART II: Beef Cow/Calf Reproductive & Nutritional Management Practices*. (1994).

54. U.S. Department of Agriculture (USDA) / Animal and Plant Health Inspection Service (APHIS). *Beef Cow/Calf Health and Productivity Audit. Forage Analyses from Cow/Calf Herds in 18 States*. (1996).

55. Johnson, K. & Cole, N. A. *Personal communication*. (2015).

56. Still, C. J., Berry, J. A., Collatz, G. J. & DeFries, R. S. Global distribution of C3 and C4 vegetation: Carbon cycle implications. *Global Biogeochem. Cycles* **17,** 1006 (2003).

57. IPCC. *Climate Change 2001: The Physical Science Basis. Contribution of Working Group I to the Third Assessment Report of the Intergovernmental Panel on Climate Change. Chapter 6*. (2001).

58. Wuebbles, D. J. & Hayhoe, K. Atmospheric methane and global change. *Earth-Science Rev.* **57,** 177–210 (2002).

59. Giglio, L., Van Der Werf, G. R., Randerson, J. T., Collatz, G. J. & Kasibhatla, P. Global

estimation of burned area using MODIS active fire observations. *Atmos. Chem. Phys.* **6,** 957–974 (2006).

60. Cerling, T. E. *et al*. Global vegetation change through the Miocene/Pliocene boundary. *Nature* **389,** 153–158 (1997).

61. Brandt, A. R. *et al*. Methane Leaks from North American Natural Gas Systems. *Sci.* **343 ,** 733–735 (2014).

62. Golding, S. D., Boreham, C. J. & Esterle, J. S. Stable isotope geochemistry of coal bed and shale gas and related production waters: A review. *Int. J. Coal Geol.* **120,** 24–40 (2013).

63. Etiope, G. & Klusman, R. W. Geologic emissions of methane to the atmosphere. *Chemosphere* **49,** 777–789 (2002).

64. Etiope, G. *Natural gas seepage: The Earth's hydrocarbon degassing*. (Springer International Publishing, 2015).

65. Etiope, G. & Ciccioli, P. Earth's degassing: a missing ethane and propane source. *Science (80-.).* **323,** 478 (2009).

66. Ntziachristos, L. *et al*. *EMEP/EEA air pollutant emission inventory guidebook 2013*. *EEA publication* (2014). doi:10.2800/92722

67. Ferretti, D. F. *et al*. Unexpected changes to the global methane budget over the past 2000 years. *Science* **309,** 1714–1717 (2005).

68. Etiope, G., Feyzullayev, A. & Baciu, C. L. Terrestrial methane seeps and mud volcanoes: A global perspective of gas origin. *Mar. Pet. Geol.* **26,** 333–344 (2009).

69. Schoell, M. & Etiope, G. Formation and migration of natural gases: Gas composition and isotopes as monitors between source, reservoir and seep. *American Geophysical Union Fall Meeting, Session H108: Tracers in Energy-related Multi-phase and Reactive Flows: Observations and Modeling, San Francisco* (2015).

70. Fung, I., Matthews, E. & Lerner, J. Atmospheric Methane Response to Biogenic Sources - Results from a 3-D Atmospheric Tracer Model. *Abstr. Pap. Am. Chem. Soc.* **193,** 6–GEOC (1987).

71. Kaplan, J. O. Wetlands at the Last Glacial Maximum: Distribution and methane emissions. *Geophys. Res. Lett.* **29,** 3–6 (2002).

72. Bergamaschi, P. *et al*. Satellite chartography of atmospheric methane from SCIAMACHY on board ENVISAT: 2. Evaluation based on inverse model simulations. *J. Geophys. Res.* **112,** 1–26 (2007).

73. Schultz, M. G. *et al*. Global wildland fire emissions from 1960 to 2000. *Global*

Biogeochem. Cycles **22,** 1–17 (2008).

74. Van Der Werf, G. R. *et al*. Interannual variability of global biomass burning emissions from 1997 to 2004. *Atmos. Chem. Phys. Discuss.* **6,** 3175–3226 (2006).

75. GFED. *Global Fire Emissions Database*. (2013).

76. Matthews, E., Fung, I. & Lerner, J. Methane emission from rice cultivation: Geographic and seasonal distribution of cultivated areas and emissions. *Global Biogeochem. Cycles* **5,** 3 (1991).

77. Houweling, S., Kaminski, T., Dentener, F., Lelieveld, J. & Heimann, M. Inverse modeling of methane sources and sinks using the adjoint of a global transport model. *J. Geophys. Res.* **104,** 26137–26160 (1999).

78. NOAA ESRL Global Monitoring Division. CarbonTracker Documentation – Convective flux fix. (2015). Available at: http://www.esrl.noaa.gov/gmd/ccgg/carbontracker/CT2013B_doc.php#tth_sEc7.2.

79. Saunois, M. *et al*. The Global Methane Budget: 2000–2012. *Earth Syst. Sci. Data Discuss.* 1–79 (2016). doi:10.5194/essd-2016-25

80. Stevens, C. M. & Engelkemeir, A. Stable carbon isotopic composition of methane from some natural and anthropogenic sources. *J. Geophys. Res.* **93,** 725 (1988).

81. Craig, H., Chou, C. C., Welhan, J. A., Stevens, C. M. & Engelkemeir, A. The isotopic composition of methane in polar ice cores. *Science (80-.).* **242,** 1535–1539 (1988).

82. Whiticar, M. in *Atmospheric Methane: Sources, Sinks, and Role in Global Change SE - 8* (ed. Khalil, M. A. K.) **13,** 138–167 (Springer Berlin Heidelberg, 1993).

83. Levin, I. in *Carbon Cycling in the Glacial Ocean: Constraints on the Ocean's Role in Global Change SE - 1* (eds. Zahn, R., Pedersen, T., Kaminski, M. & Labeyrie, L.) **17,** 3–13 (Springer Berlin Heidelberg, 1994).

84. Gupta, M., Tyler, S. & Cicerone, R. Modeling atmospheric δ13CH4 and the causes of recent changes in atmospheric CH4 amounts. *J. Geophys. Res.* **101,** 22923–22 (1996).

85. Tyler, S. C. *et al*. Stable carbon isotopic composition of atmospheric methane: A comparison of surface level and free tropospheric air. *J. Geophys. Res.* **104,** 13895 (1999).

86. Houweling, S., Dentener, F. & Lelieveld, J. Simulation of preindustrial atmospheric methane to constrain the global source strength of natural wetlands. *J. Geophys. Res.* **105,** 17243 (2000).

87. Lassey, K. R., Etheridge, D. M., Lowe, D. C., Smith, a. M. & Ferretti, D. F. Centennial evolution of the atmospheric methane budget: what do the carbon isotopes tell us? *Atmos. Chem. Phys. Discuss.* **6,** 4995–5038 (2007).

88. Neef, L., Van Weele, M. & Van Velthoven, P. Optimal estimation of the present-day global methane budget. *Global Biogeochem. Cycles* **24,** 1–10 (2010).

89. Dlugokencky, E. J., Nisbet, E. G., Fisher, R. & Lowry, D. Global atmospheric methane: budget, changes and dangers. *Philos. Trans. R. Soc. - Ser. A Math. Phys. Eng. Sci.* **369,** 2058–2072 (2011).

90. Monteil, G. *et al*. Interpreting methane variations in the past two decades using measurements of CH4 mixing ratio and isotopic composition. *Atmos. Chem. Phys.* **11,** 9141–9153 (2011).